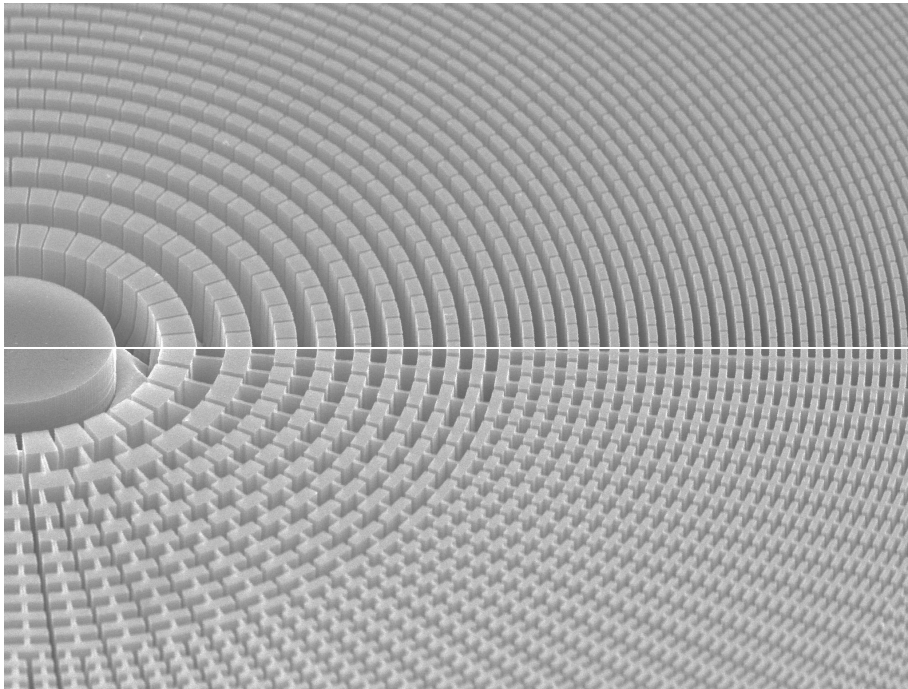


Doctoral Thesis in Physics

Metal-assisted chemical etching for nanofabrication of hard X-ray zone plates

RABIA AKAN



Metal-assisted chemical etching for nanofabrication of hard X-ray zone plates

RABIA AKAN

Academic Dissertation which, with due permission of the KTH Royal Institute of Technology, is submitted for public defence for the Degree of Doctor of Philosophy on Friday the 30th April 2021, at 10:00 a.m. in Zoom and BioX Library, Roslagstullbacken 21, Stockholm.

Doctoral Thesis in Physics
KTH Royal Institute of Technology
Stockholm, Sweden 2021

© Rabia Akan

ISBN 978-91-7873-828-1
TRITA-SCI-FOU 2021:09

Printed by: Universitetsservice US-AB, Sweden 2021

Abstract

Hard X-ray scanning microscopes, or nanoprobes, make it possible to image samples and probe their chemical, elemental and structural properties at nanoscale resolution. This is enabled by the use of nanofocusing optics. Commonly used optics in nanoprobes for high resolution X-ray experiments are zone plates.

Zone plates are circular diffraction optics with radially decreasing grating periods. Their performance depends on their geometrical properties and material. The width of the outermost zone, which today is in the order of a few tens of nanometers, defines the zone plate resolution, while the zone thickness and the material define the X-ray focusing efficiency. For hard X-ray zone plates, the required zone thickness is several micrometers. Therefore, high-aspect ratio nanostructures are a prerequisite for high-resolution, high-efficiency zone plates. The very small structures together with the high-aspect ratios make zone plates one of the most challenging devices to fabricate. A wet-chemical nanofabrication process that has proved its capability of providing silicon nanostructures with ultra-high aspect ratios is metal-assisted chemical etching (MACE). MACE is an electroless, autocatalytic pattern transfer method that uses an etching solution to selectively etch a predefined noble metal pattern into silicon. In this thesis, MACE is optimized specifically for zone plate nanostructures and used in the development of a new zone plate device nanofabrication process.

The MACE optimization for silicon zone plate nanostructures involved a systematic investigation of a wide parameter space. The preferable etching solution composition, process temperature, zone plate catalyst design and silicon type were identified. Parameter dependencies were characterized with respect to etching depth and verticality, mechanical stability of zones and silicon surface roughness.

Zone plate molds with aspect ratios of 30:1 at 30 nm zone widths were nanofabricated using the optimized MACE process. For use with hard X-rays, the silicon molds were metallized with palladium using electroless deposition (ELD). The first order diffraction efficiency of such a palladium/silicon zone plate was characterized as 1.9 %. Both MACE for the zone plate pattern transfer and ELD for the silicon mold metalization are conceptually simple, relatively low-cost and accessible methods, which opens up for further developments of zone plate device nanofabrication processes.

Sammanfattning

Hårdröntgensvepmikroskopi möjliggör avbildandet av prover och karaktärisering av dem kemiska, elementära och strukturella egenskaperna med nanometerupplösning. Detta är tack vare användandet av nanofokuserande optik. Vanligen förekommande optik i röntgenmikroskop för högupplösta analyser är zonplattor.

Zonplattor är cirkulära diffraktionsoptik med radiellt avtagande gitterperiod. Deras prestanda beror på de geometriska egenskaperna och materialet de är gjorda av. Bredden på den yttersta zonen, vilken vanligtvis är i storleksordningen av några tiotal nanometer, definierar zonplattans optiska upplösning medan zontjockleken samt dess material definierar verkningsgraden. För hårdröntgenzonplattor krävs ofta en zontjocklek på några mikrometer. Detta gör nanostrukturer med stort tjocklek-breddförhållande en förutsättning för högupplösta zonplattor med hög verkningsgrad. De väldigt små strukturerna och det stora tjocklek-breddförhållandet gör zonplattor utmanande att tillverka.

En våtkemisk nanofabriktionsprocess som har påvisat sin förmåga att tillverka kiselnanostrukturer med extrema tjocklek-breddförhållanden är metall-assisterad kemisk etsning (MACE). MACE är en elektrofri, autokatalytisk process där fördefinierade ädelmetallstrukturer med hjälp av en etslösning selektivt etsar kisel. I denna avhandling optimeras MACE specifikt för nanometerstora zonplattestrukturer och används i en ny nanofabriktionsprocess utvecklad för framtagning av zonplattor.

Optimeringen av MACE för zonplattestrukturer i kisel utgjordes av en systematisk och omfattande parameterstudie. Den bättre kompositionen av etslösningen, processtemperaturen, zonplattedesignen och kiselsubstratet identifierades. Processen karaktäriserades med avseende på zonplattans tjocklek och etsriktningen, den mekaniska stabiliteten av zoner och ytråheten hos kislet.

Kiselzonplattor med ett tjocklek-breddförhållande på 30:1 med en minsta zonbredd på 30 nm tillverkades med den optimerade MACE processen. Inför användning med hårdröntgen metalliserades kiselzonplattorna med palladium via en autokatalytisk pläteringsprocess (ELD). Verkningsgraden av första ordningens diffraktion för en sådan palladium/kiselzonplatta karaktäriserades till 1.9 %. Både MACE och ELD är konceptuellt enkla, relativt låga i kostnad och tillgängliga metoder som kommer bana väg för det vidare utvecklandet av nanofabriktionsprocesser för zonplatteframställning.

List of papers

Paper A

R. Akan, K. Parfeniukas, C. Vogt, M. S. Toprak and U. Vogt, *Reaction control of metal-assisted chemical etching for silicon-based zone plate nanostructures*, RSC Adv. **8**, 12628 (2018).

Paper B

R. Akan, K. Parfeniukas, C. Vogt, M. S. Toprak and U. Vogt, *Investigation of metal-assisted chemical etching for fabrication of silicon-based X-ray zone plates*, Microscopy and Microanalysis **24**, 286 (2018).

Paper C

R. Akan, T. Frisk, F. Lundberg, H. Ohlin, U. Johansson, K. Li, A. Sakdinawat, and U. Vogt, *Metal-assisted chemical etching and electroless deposition for fabrication of hard X-ray Pd/Si zone plates*, Micromachines **11**, 301 (2020).

Paper D

R. Akan and U. Vogt, *Optimization of metal-assisted chemical etching for deep silicon nanostructures*, manuscript, (2021).

Paper E

K. Parfeniukas, S. Giakoumidis, **R. Akan** and U. Vogt, *High-aspect ratio zone plate fabrication for hard X-ray nanoimaging*, Proc. SPIE **10386**, 103860S (2017).

List of abbreviations

AFM	Atomic force microscopy
ALD	Atomic layer deposition
CS	Central stop
DI	Deionized
DRIE	Deep reactive ion etching
EBL	Electron beam lithography
ED	Electrodeposition
ELD	Electroless deposition
FIB	Focused ion beam
HSQ	Hydrogen silsesquioxane
ICP-OES	Inductively coupled plasma optical emission spectrometry
IPA	Isopropanol
MACE	Metal-assisted chemical etching
MLL	Multilayer Laue lens
OSA	Order sorting aperture
PMMA	Poly(methyl methacrylate)
RIE	Reactive ion etching
SEM	Scanning electron microscopy

Contents

Abstract	iii
Sammanfattning	iv
List of papers	v
List of abbreviations	vi
1 Introduction	1
1.1 Nanostructured silicon	1
1.2 Objective of the thesis	2
1.3 Outlines of this thesis	2
2 NanoMAX: the hard X-ray nanoprobe of MAX IV	5
2.1 Hard X-ray nanoprobes	5
2.1.1 Focusing optics	6
2.1.2 Operation modes	6
2.2 The nanofocusing zone plate station at NanoMAX	7
3 Zone plate optics	9
3.1 Zone plate theory	9
3.2 Zone plates for the hard X-ray range	12
3.3 Fabrication methods	14
3.3.1 Direct-write processes	15
3.3.2 Etching processes	15
4 Metal-assisted chemical etching: theoretical background	17
4.1 The etching process	17
4.2 Mass-transport models	20
4.3 Etching solution	20
4.4 Temperature	22
4.5 Metal catalysts	22

4.6	Silicon	23
5	Nanofabrication of silicon-based zone plates	25
5.1	Zone plate design, patterning and deposition in gold	25
5.2	Pattern transfer with metal-assisted chemical etching	29
5.3	Metalization methods	30
5.3.1	Palladium electroless deposition	31
5.3.2	Gold electrodeposition	33
5.4	Substrate back-thinning	34
6	Optimization of metal-assisted chemical etching for zone plate nanostructures	37
6.1	Etching solution composition	38
6.2	Processing temperature	40
6.3	Zone plate catalyst design	41
6.4	Silicon type	44
7	Zone plate efficiency characterization	47
7.1	Experimental setup	47
7.2	First order diffraction efficiency quantification	48
8	Conclusions and outlook	51
	Summary of papers	53
	Acknowledgements	55
	Bibliography	57

Chapter 1

Introduction

1.1 Nanostructured silicon

The research fields of medicine [1], photonics [2,3], thermoelectrics [4], photovoltaics [5,6], energy storage [7,8] and X-ray optics [9] might at the first glance seem very distant from each other. What could possibly be the common denominator that gathers thermoelectric materials, membranes for drug delivery and Fresnel zone plates in the same list? The answer is nanostructured silicon.

By accident, porous silicon was discovered by Arthur Uhlir and Ingeborg Uhlir in 1956 during one of their electro-polishing experiments [10]. The discovery found great attention years later, in the early 1990s, when Canham reported a strong and bright photoluminescence from porous silicon at room temperature [11]. Since then, different fabrication methods for this interesting nanostructured material have been investigated. In 1997, the first report came of an electroless etching method catalyzed by aluminium for the selective formation of porous silicon layers in an acid-mixture consisting of nitric and hydrofluoric acid [12]. Shortly after, the aluminium was exchanged to a noble metal that stayed inert in an etching solution composed of hydrogen peroxide and hydrofluoric acid and produced porous silicon defined by the morphology of the noble metal catalyst [13]. This report by Li and Bohn is considered as the first study that introduced metal-assisted chemical etching (MACE, MacEtch or MAE), not only as a method to form porous silicon, but silicon with defined 3D nano- and micro-structure morphology. Since its discovery, MACE has shown its diversity and capability as a new method for the fabrication of advanced silicon structures for a wide range of applications that require high aspect ratios, i.e., structures with large thicknesses in relation to their structural widths [14–16].

One application that requires ultra-high aspect ratio silicon nanostruc-

tures are a special type of X-ray optics: Fresnel zone plates [17, 18]. For the fabrication of hard X-ray zone plate optics, nanostructures around tens of nanometers with lengths of several micrometers and aspect ratios of at least 30:1 are needed. Zone plate devices are commonly used in hard X-ray scanning microscopes as imaging and nanofocusing optics [19]. Hard X-ray microscopy enables non-invasive analysis of matter, where not only information about the surface of an object can be gathered but also its interior. Probing properties of matter at nanoscale, or even atomic scale resolution would help us understand and answer important questions in materials science, life science, earth science, nanoscience and many others. The limitations in the achievable aspect ratios of these optics has been the limiting factor at what scale analyses can be performed with X-ray microscopy. The optical resolution of such a tool depends on the size of the focused X-ray spot which is defined by the structural sizes of the zone plate. Processes for high-aspect ratio zone plate structures are needed for the continued development of hard X-ray microscopy. And this is exactly what we try to do in this thesis: process development for the nanofabrication of high-aspect ratio zone plate nanostructures using MACE for the improvement of hard X-ray scanning microscopy.

1.2 Objective of the thesis

This thesis work aims to explore MACE as a pattern transfer method to fabricate high-aspect ratio silicon nanostructures, specifically zone plates. The objective is to identify the dependencies between experimental MACE parameters and etching verticality, mechanical stability and silicon wall roughness and optimize the process for the development of a zone plate device nanofabrication process.

1.3 Outlines of this thesis

After the present introduction, this thesis is structured as follows.

Chapter 2 introduces the concept of X-ray scanning microscopy and gives a general overview of such a setup. NanoMAX, the hard X-ray nanoprobe of MAX IV, is presented and its nanofocusing zone plate station is described.

Chapter 3 covers the basic theory about zone plate optics. Their required properties to function with hard X-rays are detailed and an overview of the commonly used fabrication processes are listed. Recent advances in the nanofabrication field are presented, including MACE.

Chapter 4 provides a theoretical background about MACE and discusses the expected influence of the involved process parameters on the etching behaviour.

Chapter 5 presents a step-by-step description of the nanofabrication process used for zone plate device fabrication. Critical considerations about each part of the process are provided.

Chapter 6 describes the MACE optimization of zone plate nanostructures. The systematically explored parameters and their influence on the etching outcome is thoroughly discussed.

Chapter 7 summarizes the first order diffraction efficiency characterization of the zone plate devices fabricated via the developed nanofabrication process.

Chapter 8 concludes this thesis work and gives a brief outlook on potential developments for the future.

Chapter 2

NanoMAX: the hard X-ray nanoprobe of MAX IV

Hard X-ray scanning microscopy is an imaging- and analysis method that enables sample imaging and probing their properties at the nanoscale. This combination makes hard X-ray microscopy attractive to various fields of physics, chemistry and biology, including materials science, life science, earth science, nanoscience and many others. Thanks to the large penetration depth of X-rays, hard X-ray microscopy has the strength of examining the sample interior without any need for destructive sample preparation. All this is possible by illuminating the sample with a nanofocused, hard X-ray spot. This chapter introduces the concept of hard X-ray scanning microscopes, also called nanoprobe, and focuses especially on the NanoMAX beamline at MAX IV.

2.1 Hard X-ray nanoprobe

The main components of an X-ray nanoprobe are an X-ray light source, optic to produce an intense spot and focus the photons on the sample, a scanning stage holding the sample and a detector to record an image or other sample properties. Synchrotron facilities are typically used as X-ray sources in high performance nanoprobe due to their capability to deliver stable X-ray beams with high flux. In practice, a synchrotron light source could be used to perform transmission imaging of an object without the use of any optical device. However, optics are necessary to probe local sample properties at nanoscale resolution. For this, reflective, refractive and diffractive optics are used.

2.1.1 Focusing optics

Kirkpatrick-Baez (KB) mirrors are widely used at synchrotron facilities and focus the incoming beam by reflection in both horizontal and vertical directions [20]. The advantage of this arrangement is the high focusing efficiency that can reach up to 90% [21]. However, the size of the focused X-ray spot is limited to around 100 nm at hard X-ray energies of 10 keV and lower [22].

Refractive optics, or lenses, have also been proposed as nanofocusing optics [23]. Due to the impractically long focal length of a single lens, stacking of multiple lenses or compound lens setups have been used [24, 25]. Multiple lenses etched into a single device gives short focal lengths, but severely limits the focusing efficiency. To avoid absorption losses, light atomic number materials are used for lenses [26].

Fresnel zone plates [17] and Multilayer Laue lenses (MLLs) [27] are two types of diffractive optics. Zone plates are circular gratings with radially decreasing line width so that the X-rays are diffracted into a common focal point (described in more detail in Chapter 3) [28]. Their high resolution and ease-of-use make zone plates often the optics of choice at synchrotron nanoprobe, however, with a disadvantage of low focusing efficiency. The maximum theoretical efficiency of standard hard X-ray zone plates is 40% [29]. Frequent improvements in nanofabrication tools and processes are nonetheless pushing the limits of achievable resolution and practical efficiency of zone plates.

As the name suggests, MLLs consist of multiple layers of alternating materials with decreasing thicknesses over the device. A large number of layers are required in these devices, which can be in 1D or 2D. The fabrication is the biggest limitation here due to the required accurate control during deposition of the materials. However, MLLs can be fabricated with arbitrary thicknesses, nanometer sized layers and even tilted zones, overcoming the diffraction efficiency and resolution limits of normal zone plates [30].

2.1.2 Operation modes

Nanoprobes are highly flexible tools that can be operated in several modes to record chemical, elemental and structural information about both the surface and interior of a sample as a function of sample position [18]. Transmission spectrum analysis, also referred to as spectromicroscopy, records the X-ray absorption at a set wavelength and yields spectroscopic information. Within a heterogeneous sample, the chemical state and coordination number of an element can be analyzed while structural imaging of relatively thick samples can be done [31]. Fluorescence is a second operation mode [32]. Here, the elemental composition of a sample can be examined by analyzing the resulting emission caused by the incident X-ray beam. A third operation

mode involves analysis of photoelectron emission [33]. Combined with photoemission spectroscopy, characterization of the sample surface chemistry can be performed. Lastly, detection of diffracted photons gives structural information about the sample.

2.2 The nanofocusing zone plate station at NanoMAX

The modern Swedish synchrotron MAX IV is today one of the brightest synchrotron light sources [35]. The NanoMAX beamline of MAX IV hosts two hard X-ray nanoprobe. This thesis investigates nanofocusing zone plate optics especially designed for NanoMAX. NanoMAX operates routinely at energies between 8 - 15 keV (0.15 - 0.083 nm) and in-situ, in-vivo and in-operando 2D and 3D mapping experiments are offered to users [34]. Today, one of the two nanoprobe of NanoMAX, the KB-mirror experimental station, is open for users. The other experimental station at NanoMAX will be the nanofocusing zone plate station. A layout of the NanoMAX beamline is illustrated in Figure 2.1. The figure shows the X-ray beam being generated in the undulator and then passing through different optical devices before it reaches the experimental stations: the two hard X-ray nanoprobe.

The nanofocusing zone plate station is currently in a design phase and first experiments are expected in 2022. The final optical device in this setup is a Fresnel zone plate which focuses the X-ray beam to nanoscale before it illuminates the sample. The design and dimensions of the zone plate device determine the size of the nanofocused X-ray beam, and further the resolution of the hard X-ray nanoprobe. The basis for this thesis is the nanofabrication of hard X-ray zone plates for 8 - 10 keV (0.15 - 0.12 nm)

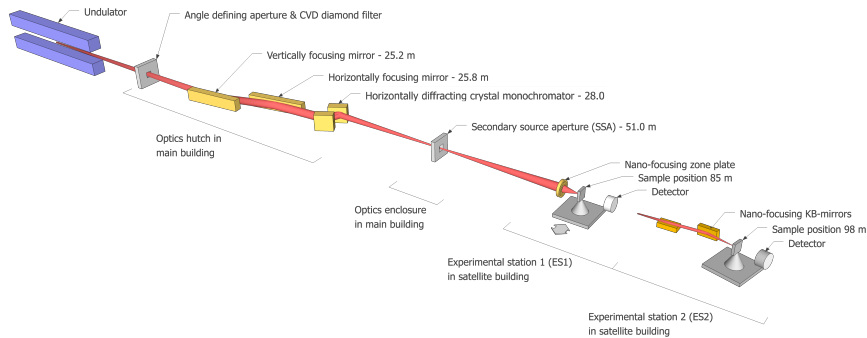


Figure 2.1. Layout of the NanoMAX beamline and its two hard X-ray nanoprobe [34].

use, especially for the nanofocusing zone plate station of NanoMAX.

Chapter 3

Zone plate optics

Zone plates are often used as optics to focus X-rays to nanoscale-sized spots. A zone plate is a circular diffraction grating that consists of several alternating opaque or phase-shifting and transparent rings, called 'zones'. The zone widths are decreasing with the zone plate radius so that the incoming X-rays are focused to a common focal point. The zone plate geometry, zone height and zone plate material will determine the performance of the optic at a specific X-ray wavelength. The principle behind zone plates, specific properties they should have to function in the hard X-ray range and different fabrication methods are presented and discussed in this chapter.

3.1 Zone plate theory

The main function of a zone plate is to diffract light so it interferes constructively at the focal point. This is accomplished by cancelling the destructively interfering light with opaque zones or alternatively phase-shift the light by a factor of π . The symmetry of equal areas of every alternating zone pair (opaque/phase-shifting and transparent) is a prerequisite for a zone plate. Odd zones will be of a light enough material so X-rays can transmit through and even zones will be of a highly absorbing or phase-shifting material, or vice versa. A zone plate with opaque zones and with equally wide lines and spaces (line-to-space ratio = 1) diffracts the incoming light into different diffraction orders m as [18]

$$\eta_m = \begin{cases} 0.25 & m = 0 \\ 1/m^2\pi^2 & m \text{ odd} \\ 0 & m \text{ even} \end{cases}$$

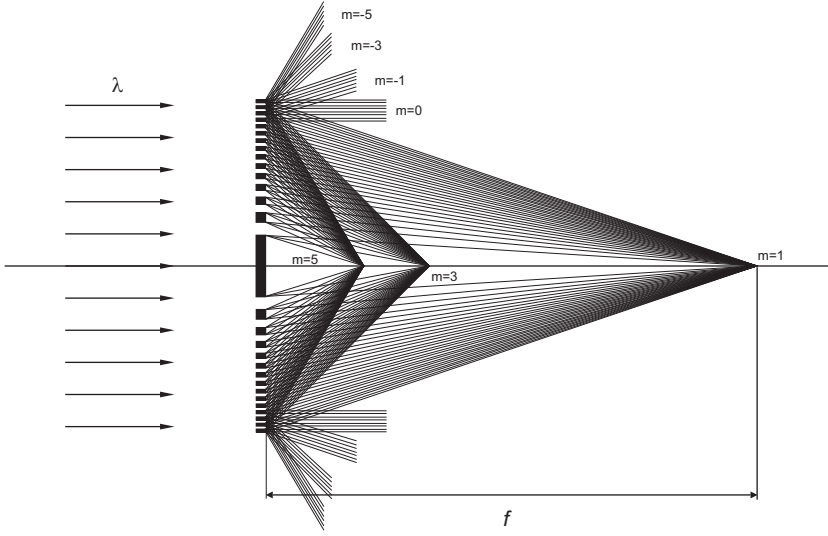


Figure 3.1. Zone plate focusing into the first three odd diffraction orders. The even diffraction orders are cancelled out for a zone plate with line-to-space ratio equal to 1. The focal length for the first diffraction order ($m=1$) is denoted f . Negative diffraction orders originate from virtual foci behind the zone plate. The first three negative orders and the transmission rays ($m=0$) are indicated for the outermost zones for clarity. Figure used with permission from A. Holmberg [36].

Figure 3.1 illustrates how the incoming light is diffracted into the different orders. Half of the incoming light is absorbed in the zone plate itself, 25% ends up in the 0th order and approximately 10% is diffracted in the 1st order. The latter number can for a given X-ray wavelength get as high as 40% for zone plates with a phase-shifting material (discussed in 3.2).

Only considering the first diffraction order, the squared radius of the n th zone is expressed as

$$r_n^2 = n\lambda\left(f + \frac{n\lambda}{4}\right)$$

where λ is the X-ray wavelength and f is the zone plate focal length. The larger the number of n is, the further out on the zone plate the zone is and the smaller its width (Figure 3.2). For zone plates, f is often larger than $\frac{n\lambda}{4}$ such that

$$r_n \simeq \sqrt{n\lambda f}$$

The total number of zones in a zone plate is denoted N , and the N th zone is the outermost and the thinnest one. The radius of a zone plate with

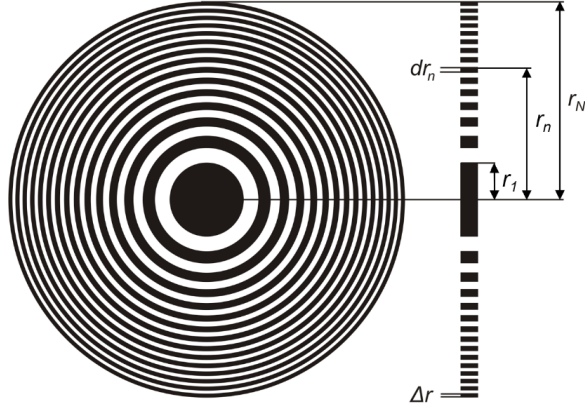


Figure 3.2. Zone plate with N zones. The radius of the first, n th and outermost zone N are denoted r_1 , r_n and r_N , respectively. The width of the n th zone is dr_n and the outermost zone width is Δr . Figure used with permission from K. Parfeniukas [37].

N zones will therefore be

$$r_N \simeq \sqrt{N\lambda f}$$

The total number of zones, N , and the width of the outermost zone, Δr , are two important geometrical parameters involved in the focusing performance of a zone plate optic. In fact, the resolution of the zone plate optic is set by the width of the outermost zone

$$\Delta r \simeq \frac{\lambda f}{2r_N} = \frac{\lambda}{2NA}$$

where NA is the numerical aperture of the zone plate. A combination of these expressions shows that the number of zones in a zone plate is inversely square proportional to its resolution

$$N = \frac{r_N^2}{\lambda f} = \frac{\lambda f}{4\Delta r^2}$$

From a fabrication point of view, this means that a doubling of the resolution, i.e., halving the outermost zone width, will require the quadrupling of the number of zones. In some cases the diameter of the zone plate has to match the size of an incident beam. Then, the number of zones has to be adjusted accordingly. The smaller the outermost zone width, the better the zone plate resolution and hence the more challenging the fabrication.

So far, geometrical factors of the zone plate optic have been described. There are, however, certain restrictions the X-ray light source puts for the zone plate to reach its diffraction-limited performance. In the ideal case, a completely monochromatic light source should be used. Real sources have however an intrinsic spectral band width, $\Delta\lambda$, which has to be taken into account and restricts the maximum number of zones in a zone plate so that

$$\frac{\Delta\lambda}{\lambda} \leq \frac{1}{N}$$

In order to get as good imaging performance as possible, the shift in focus caused by the source bandwidth $\Delta\lambda$ should be less than the depth of focus, DOF, of the system

$$\text{DOF} = \pm \frac{\lambda}{2NA^2}$$

To summarize, the following parameters are taken into account when designing zone plate optics: the symmetry and equal area of alternating zone pairs, the intended X-ray wavelength of use (λ), the zone plate radius (r_N), the number of zones (N) and the desired resolution, i.e., outermost zone width (Δr).

3.2 Zone plates for the hard X-ray range

Until now, this chapter has introduced zone plate properties mainly with respect to its geometry. When the X-ray wavelength and the design of the zone plate is decided upon it is time to find a zone plate material that gives the best focusing efficiency.

In the EUV and X-ray range, the complex refractive index is described as

$$n = 1 - \delta + i\beta$$

where δ and β are its real and imaginary components affecting the phase shift and absorption in the zone plate material, respectively. A higher first order diffraction efficiency than for zone plates with opaque zones is obtained by instead choosing a phase-shifting, partly transmitting material. This will reduce the absorptive photon losses. A phase shift of π will yield a maximum first order diffraction efficiency and the required thickness, or zone height, for a given wavelength and material is

$$t = \frac{\lambda}{2\delta}$$

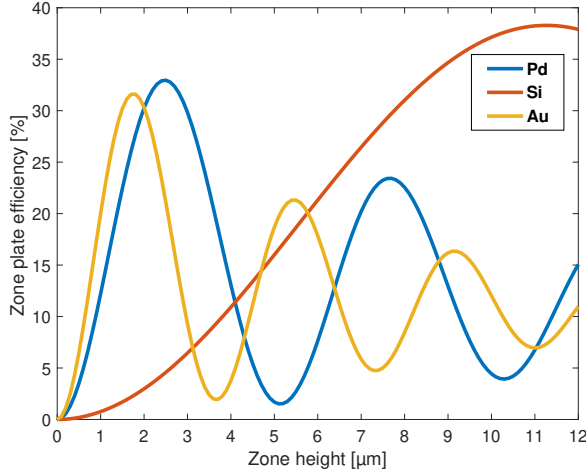


Figure 3.3. First order diffraction efficiency as function of zone height for palladium, silicon and gold zone plates at 9 keV photon energy. Calculations were done in MATLAB using GD-Calc [38].

The zone plate first order diffraction efficiency takes into account both the real and imaginary parts of the refractive index and can be expressed as [29]

$$\eta = \frac{1}{\pi^2} (1 + e^{-4\pi\beta t/\lambda} - 2e^{-2\pi\beta t/\lambda}) \cos(2\pi\delta t/\lambda)$$

The first order diffraction efficiency will reach its theoretical maximum by choosing a material with a β/δ ratio as small as possible and with a thickness giving a phase shift approaching π .

Figure 3.3 shows the variation of the first order diffraction efficiency with zone height of palladium, silicon and gold zone plates at 9 keV (0.14 nm). Palladium, silicon and gold zone plates reach their maximum theoretical efficiencies at zone heights of 2.5 μm , 11 μm and 1.8 μm , respectively. Even though their maximum theoretical efficiencies are lower than for silicon, palladium or gold would be suitable as zone plate materials for 9 keV use. Especially, their smaller zone heights, together with a small zone width for resolution, would be more feasible from a fabrication perspective. Instead, silicon that requires extreme aspect ratios at hard X-ray wavelengths, would be a good material to use as a mold for other, more opaque materials as palladium or gold.

This scenario is illustrated in Figure 3.4. Using silicon as a mold for these high-Z materials results in slightly lower theoretical first order diffraction efficiencies. A combined palladium/silicon zone plate reaches its maximum

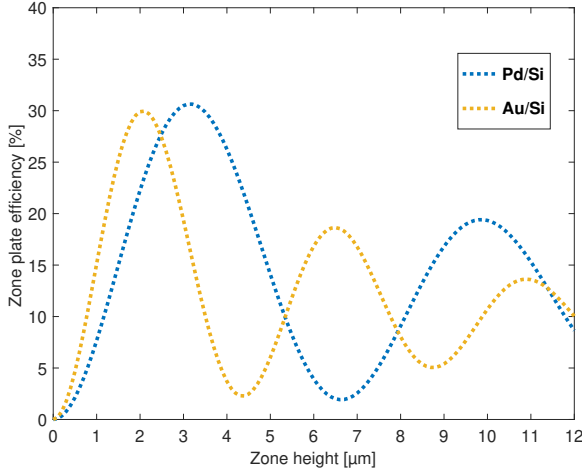


Figure 3.4. First order diffraction efficiency as function of zone height for combined palladium/silicon and gold/silicon zone plates at 9 keV photon energy. Calculations were done in MATLAB using GD-Calc [38].

focusing efficiency at 3.3 μm and a gold/silicon zone plate at 2 μm ., i.e., at larger zone heights than pure palladium or gold zone plates. Both a lower first order diffraction efficiency and slightly thicker zones for a dual-material zone plate might seem unnecessary. However, using silicon as molds can provide mechanical stability to high-Z nanostructures. To conclude, it is not only the theoretical diffraction efficiency that is taken into account for the choice of zone plate material, but the availability in fabrication methods to manufacture high-aspect ratio, mechanically stable nanostructures.

3.3 Fabrication methods

Zone plate fabrication can be divided into two approaches: direct-write and etching processes. Independent of what approach is chosen for fabrication of the zone plate device, the first step in most modern zone plate fabrication methods is to define the pattern using electron beam lithography (EBL). EBL offers high resolution and good flexibility in the patterning process, and uses an electron sensitive polymer layer, or e-beam resist, in which the pattern is written. The following processing steps are then dependent on the intended X-ray wavelength of use and the desired aspect ratios.

3.3.1 Direct-write processes

Direct-write processes use the zone plate patterned e-beam resist as mold for high-Z, phase-shifting materials. The achievable aspect ratios using direct-writing are limited due to electron forward scattering in thick e-beam resist layers. This makes the direct-write approach very suitable for soft X-ray zone plates that do not require as large zone heights as zone plates for hard X-ray wavelengths. There are two main methods that are included in the direct-write approach.

The first method uses a 1:1 line-to-space ratio zone plate design exposed in a positive resist, commonly poly(methyl methacrylate) (PMMA) [39]. In a positive resist the e-beam exposed polymer chains are fragmented into shorter fractions that are removed upon development. Electrodeposition (ED) is used to fill the mold with a high-Z and phase-shifting material, commonly gold or nickel [40]. Typically, silicon nitride membranes coated with a thin conductive plating base layer are used as substrates.

The second method uses a 1:3 line-to-space ratio zone plate design exposed in the negative, silicon-based resist hydrogen silsesquioxane (HSQ) [41]. In contrast to positive resists, the e-beam exposed chains in a negative resist are cross-linking and the unexposed resist is removed upon development. Larger zone heights can be obtained with HSQ than for a positive resist thanks to superior mechanical stability. Atomic layer deposition (ALD) is used to conformally coat the free-standing zones with a high-Z and phase-shifting material, e.g., iridium or platinum. Silicon nitride membranes are commonly used as substrates with this method.

The direct-write approach comes with the advantage of few processing steps and the disadvantage of small zone heights. One way to improve the zone thickness is to process both sides of the membrane [42] or stack multiple zone plates together [43,44]. In both cases the alignment has to be very accurate and done with high precision [45].

3.3.2 Etching processes

Compared to the direct-writing approach, etching processes use thinner resist layers for the zone plate patterning. The EBL patterning becomes easier due to this, which is one of the advantages with the etching approach. Instead, the defined pattern is transferred into a substrate material. Etching processes for zone plate fabrication are categorised as reactive ion etching (RIE) and MACE.

RIE is a dry etching method that uses plasma for the pattern transfer. Here, an etch-resistant mask is used to selectively and anisotropically etch the substrate material that is not covered by the mask. The etched material is either a low-Z material that serves as mold for an electrodeposited high-Z

material, or a high-Z, phase-shifting material that is directly etched. Polyimides are examples of a polymeric, low-Z materials that have served as zone plate mold for nickel ED [46], and tungsten and germanium are examples of materials that have been processed with RIE and used directly as a zone plate devices [47,48]. In both cases, the material to be etched is deposited on a supportive substrate, commonly a silicon nitride membrane. Difficulties in nanostructure etching with a maintained vertical etching profile has led to limited possibility for improvement of the RIE process for zone plate fabrication. Instead, MACE has been shown to be a good alternative for fabrication of high-aspect ratio zone plate nanostructures with vertical etch profiles [49].

MACE is performed in both liquid-phase and gas-phase for zone plate fabrication [9]. Silicon is typically the substrate material used in MACE. After defining a 1:1 or 1:3 line-to-space ratio zone plate pattern in a positive resist, a noble metal layer is deposited onto the silicon and the resist is removed in a lift-off process. The noble metal patterned silicon substrate is immersed in an etching solution or exposed to a gas-mixture consisting of hydrofluoric acid (HF) and an oxidant. The noble metal catalyzes the MACE reaction and anisotropically etches the silicon, transferring the zone plate pattern into the substrate. The 1:1 line-to-space ratio silicon zone plate mold is filled with a high-Z, phase-shifting material using ED or electroless deposition (ELD), typically gold or palladium [50]. The 1:3 line-to-space ratio structures are instead coated conformally using ALD, commonly with platinum [49,51].

MACE comes with the advantage and capability to fabricate high-aspect ratio nanostructures while maintaining etch verticality [52]. This makes this process attractive to various applications. MACE is a relatively new method for zone plate fabrication and the effect of the different process parameters on the resulting zone plate structures is unclear. This lends to the main goal of this thesis: to identify the most important etching parameters and investigate their influence on liquid-phase MACE of zone plate nanostructures.

Chapter 4

Metal-assisted chemical etching: theoretical background

As introduced in the previous chapters, MACE opens up the possibility to fabricate high-aspect ratio zone plate nanostructures in silicon. The main method of focus in this thesis is liquid-phase MACE. To understand how different experimental parameters involved in MACE will affect the zone plate etching, a description of the process theory is needed. In this chapter an overview of the etching process is introduced in 4.1; different mass transfer mechanisms are discussed in 4.2; the etching solution composition and the role of each component are in 4.3; the influence of the etching temperature is in 4.4; metal catalysts and their morphological effect on the etching are described in 4.5; and finally, influence of the silicon substrate properties are brought up in 4.6.

4.1 The etching process

Since its discovery in 2000 by Li and Bohn [13], MACE has been used for the fabrication of silicon-based nanostructures for a variety of applications. Advantages of the method are its relatively low cost, simplicity and accessibility compared to other competing pattern transfer techniques. No sophisticated equipment is needed for the process and it can be performed in a chemistry laboratory. It was first introduced as a zone plate fabrication method in 2014 by Chang and Sakdinawat [49] and has since then been employed not only for hard X-ray zone plates [50, 51, 53–57], but also for other diffractive X-ray optics [58, 59].

MACE is a mixed chemical and electroless etching process [60]. In a typical MACE experiment, a noble metal patterned silicon substrate is exposed to an etching solution consisting of HF and a strong oxidant. The

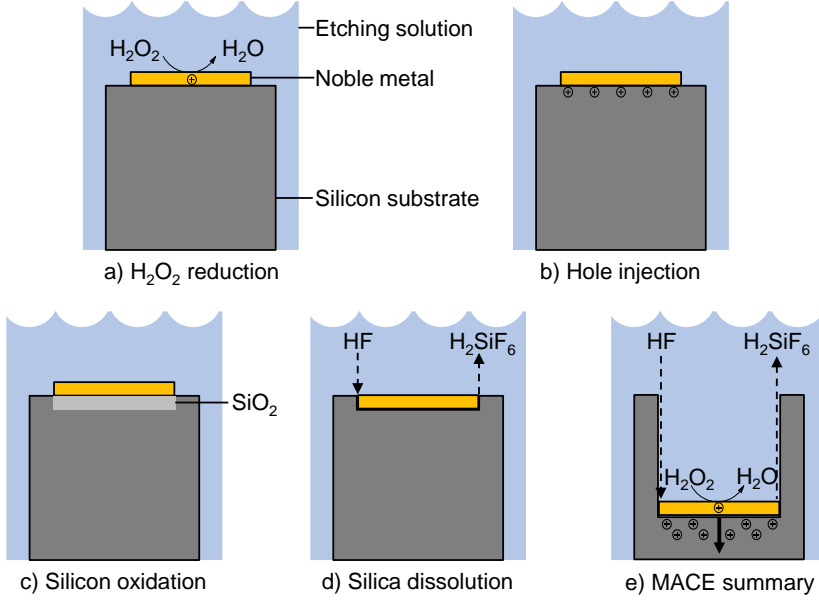
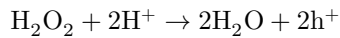


Figure 4.1. Schematic illustration of the MACE process. a) The oxidant H_2O_2 is reduced at the noble metal surface and holes are formed as a result. b) The formed holes are injected into the silicon at the noble metal/silicon interface. c) The silicon is oxidized. d) The oxide layer is dissolved by HF . e) The steps in a)-d) are repeated and the noble metal catalyst is transferred into the silicon substrate.

silicon beneath the noble metal is typically etched much faster than the silicon without any noble metal coverage thanks to the catalytic activity of the metal. Without a noble metal catalyst, the etch rate of silicon is below 10 nm/h [61]. The morphology of the etched silicon is mainly defined by the morphology of the noble metal catalyst. For simplicity, the MACE process described in this section is based on the assumption that a silicon substrate patterned with an isolated noble metal catalyst layer is etched in an etching solution composed of HF and the oxidant hydrogen peroxide (H_2O_2).

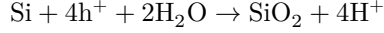
In the MACE process, there is a cathode site (noble metal surface) and an anode site (silicon surface) with local hole currents flowing between them. The H_2O_2 is reduced at the noble metal catalyst surface as follows



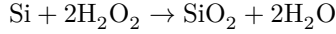
This cathode reaction is well accepted as the first step in the MACE process. The generated holes are injected into the silicon substrate at the noble

metal/silicon interface. There are, however, several proposed mechanisms in the literature describing the anode reaction [16]. Figure 4.1 is a schematic illustration of one of these mechanisms [60, 62, 63].

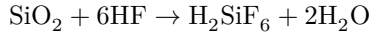
First, the silicon is oxidized to form silica as a result of the hole injection



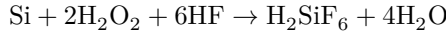
The balanced redox reaction at the noble metal/silicon interface is



Following the hole injection and oxidation of silicon, the formed silica is dissolved by HF



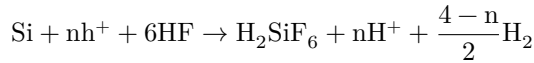
A combination of the redox reaction and the silica dissolution reaction gives the following overall MACE reaction



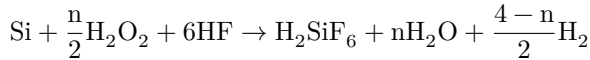
Other proposed anode reaction mechanisms include direct dissolution of silicon. The mechanism proposed for direct dissolution of silicon in tetravalent state is [13, 64]



and a proposed general mechanism is [60]



with n ranging from 2 to 4. Taking the cathode reaction into account, the overall MACE reaction can be expressed as



To summarize, there is no established MACE reaction mechanism due to difficulties in analyzing the surface state of silicon in-situ. Ex-situ analysis will be uncertain due to the formation of native oxide on silicon in the atmosphere. Today, the generally accepted MACE process is: (1) The oxidant is predominantly reduced at the surface of the noble metal catalyst and holes are formed. (2) The holes diffuse through the noble metal layer and are injected into the silicon. The hole concentration is largest at the

noble metal/silicon interface. (3) The silicon is oxidized upon injection of holes. (4) The oxidized silicon is dissolved by HF and the byproducts resulting from the dissolution are transferred from the reaction site. There are different models proposed on how the mass-transport to and from the reaction site is taking place.

4.2 Mass-transport models

There are three models proposed for the transport of reagents to and byproducts from the MACE reaction site, as illustrated in Figure 4.2. Model I and Model II suggest a mass-transport occurring at the noble metal/silicon interface, while Model III proposes that the etching occurs at the noble metal surface.

In Model I, the catalyst is continuous and the transport of reagents and byproducts occurs along the metal/silicon boundaries [61]. The reagent/byproduct diffusion length is mainly determined by the lateral size of the catalyst layer. The larger the catalyst pattern, the slower the etching due to limited diffusion and vice versa.

In Model II, the catalyst is porous and the transport of the reagents and byproducts occurs through the pores in the metal [65]. In contrast to Model I, the reagent/byproduct diffusion length in Model II is determined by the thickness of the catalyst layer. Hence, the thicker the catalyst layer the slower the etching due to slower diffusion and vice versa.

In Model III, silicon atoms diffuse through the catalyst layer to the catalyst surface [16]. The basis for this proposal is the tendency of silicon to mix into metals by diffusion [66,67]. While at the surface of the noble metal, the silicon atoms are oxidized and further dissolved. According to this model, the etching rate is determined by the thickness of the catalyst layer.

Studies have been conducted to identify how the mass-transport occurs [61,68]. The difficulties in in-situ and ex-situ analyses limit the classification of the mass-transport model. MACE occurs both with a thick, continuous metal catalyst with no pores and with thin, porous metal catalysts. Thus, pores in the metal catalyst is not a prerequisite for the MACE reaction (oxidation and dissolution of silicon) to occur, but facilitates the mass-transport especially for catalysts in the microscale [69].

4.3 Etching solution

In section 4.1 the MACE process was introduced based on an etching solution with H_2O_2 as the oxidant. An etching solution consisting of H_2O_2 and HF is by far the most frequently reported composition used in MACE.

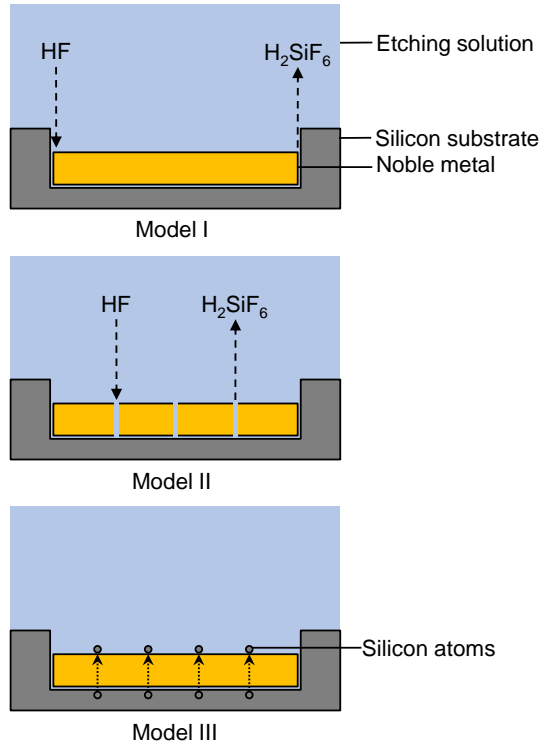


Figure 4.2. Schematic illustration of the three proposed models for mass transport during MACE. In Model I, the reagents and byproducts diffuse along the noble metal/silicon interface. In Model II, the reagents and byproducts diffuse through pores in the noble metal catalyst. In Model III, silicon atoms from the substrate diffuse through the noble metal catalyst and gets oxidized and dissolved on the noble metal surface.

Also, it is the etching solution composition used in this thesis. It is however worth mentioning that other oxidants are used as well, e.g., nitric acid and metal salts [70].

The concentrations of H_2O_2 and HF affect both the etch rate and the morphology of the etched structures. It is suggested that the hole injection rate is controlled by the concentration of H_2O_2 while the HF concentration regulates the silicon dissolution rate [16]. A balance between the hole injection and dissolution rates will, based on this, result in the metal catalyst pattern being transferred into the silicon without any morphological changes. When the hole injection rate is faster than the dissolution rate, i.e., concentration of H_2O_2 too high, a surplus of holes are present at the

noble metal/silicon interface. These holes can diffuse away in an uncontrolled manner, oxidize and subsequently etch other sites on the silicon, as illustrated in Figure 4.3. This introduces a certain degree of porosity to the surrounding silicon structures [54].

Alcohol additives in the etching solution do not take part in the etching reaction but influence the etching outcome. The effect of isopropanol (IPA) has shown to reduce the etch rate, improve the etching uniformity over large catalyst areas and reduce porosity formed as a consequence of off-site etching [59, 71]. Furthermore, large concentrations of alcohol additives influence the curvature of etched silicon nanostructures [72, 73].

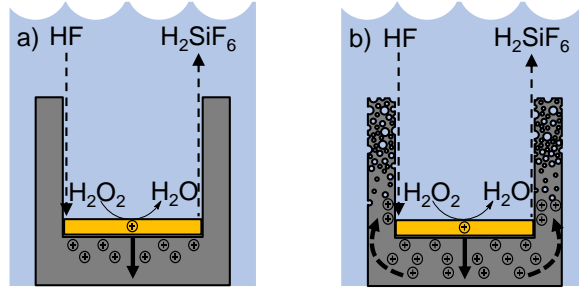


Figure 4.3. Schematic illustration of the hole injection rate a) in balance with the silicon dissolution rate resulting in hole consumption at the noble metal/silicon interface, and b) higher than the hole consumption rate at the noble metal/silicon interface resulting in holes diffusing to other sites of the silicon followed by oxidation and dissolution of those sites.

4.4 Temperature

The etching temperature is believed to have a similar effect on the MACE reaction kinetics as the concentration of the etching solution. The overall etch rate (oxidation and dissolution) will increase with temperature due to the provided energy to the system and result in deeper transfer of the noble metal catalyst pattern into the silicon substrate [16, 74, 75]. The increase in temperature also comes with the side effect of an off-site etching, similarly to the effect of the oxidation rate described in 4.3 [54, 75].

4.5 Metal catalysts

Noble metals are used in MACE for fabrication of structures with defined morphology. The reason for this is their ability to preserve their structures without dissolving in the etching solution. Commonly used noble metals

are silver, gold, platinum and palladium [16]. Gold is used as the catalyst metal in this thesis. Non-noble transition metals have also been used in MACE, but to form porous silicon and for surface polishing [70].

Catalysts in a variety of shapes and sizes have been employed in MACE (examples presented in Figure 4.4). The deposition of the metal onto the silicon is performed in multiple ways depending on the final application of the etched structures. For defined patterns in the nanoscale, EBL is combined with electron beam evaporation for deposition of the catalyst. Other methods include nanosphere lithography combined with evaporation to form close-packed dot arrays and ELD of a metal precursor to form nanoparticles, dendrites and continuous or discontinuous films [70].

MACE of lithographically defined catalyst patterns often needs to be controlled and follow a defined etching direction. Vertical etching is for instance of high importance for zone plate fabrication. Etching verticality is favored by an interconnected catalyst pattern providing a collective etching into the silicon substrate. Isolated catalysts, especially in the nanoscale, tend to etch in an uncontrolled manner due to their freedom of movement. Substrate surface defects or facets in the catalyst tend to have a bigger impact on the course of the etching of catalysts in the nanoscale than catalysts in the microscale.

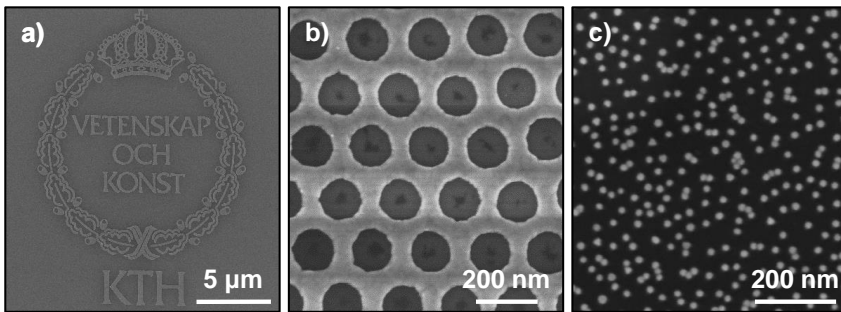


Figure 4.4. Scanning electron microscopy (SEM) micrographs of different catalyst morphologies. Light parts are gold and dark parts are silicon. a) KTH Royal Institute of Technology logo defined with EBL. b) Dot array defined by nanosphere lithography. c) Nanoparticles.

4.6 Silicon

Among all conditions involved in MACE, the silicon doping type has shown a minor effect on the etching outcome [70]. The etching process is in other words independent of if the substrate is p- or n-type. On the other hand,

the doping concentration is critical and shows a great influence on the etch morphology. The higher the doping concentration of the starting silicon substrate, the greater the post-etch porosity degree and surface roughness [76–79].

Generally in MACE, at low etch rates the preferential anisotropic etch trend is vertical along the $\langle 100 \rangle$ direction irrespective of the substrate crystal orientation [16, 70]. According to the back-bond strength theory, a weakening of the silicon back-bonds in the $\langle 100 \rangle$ is stronger than it is for other directions since there is the lowest density of back-bonds to be broken [63]. The effective back-bond number density increases with $(100)\langle 110 \rangle \langle 111 \rangle$ [9]. As a consequence, less energy is required to etch the silicon along the $\langle 100 \rangle$ direction. However, etching along non- $\langle 100 \rangle$ directions have been reported at extremely high etch rates, suggesting a correlation between the etch rate and direction [73, 80]. Breaking of higher density back-bonds can thus be kinetically favored at sufficiently high etch rates.

Summary

In this chapter the fundamentals of MACE have been explored. Different theories on how the etching occurs have been presented and the effects of etching solution composition, temperature, metal catalyst and properties of the silicon substrate have been discussed. These topics will serve as a basis for later discussions on the influence of MACE parameters on zone plate etching in Chapter 6. Before that, the overall fabrication process of zone plate devices will be presented in Chapter 5.

Chapter 5

Nanofabrication of silicon-based zone plates

In this chapter, all steps for the fabrication of silicon-based zone plates are presented. The described process starts with a silicon substrate and ends with a zone plate device ready to be used in a hard X-ray nanoprobe setup. The overall zone plate fabrication method involves four main parts: (1) Zone plate design, patterning by e-beam lithography and gold deposition onto silicon, (2) pattern transfer via MACE into substrate to form a zone plate mold, (3) metalization of the mold, and (4) back-thinning of substrate. Each part has its own set of parameters and considerations that are thoroughly analyzed in its respective section. The main points of this chapter formed the basis for the work presented in Paper C.

5.1 Zone plate design, patterning and deposition in gold

The first part of the zone plate device fabrication is illustrated in Figure 5.1 a)-d) and prepares the substrate for MACE. When designing zone plates for fabrication with MACE, etching verticality and mechanical stability has to be taken into account. The etching gets more homogeneous when the zones in the catalyst pattern are interconnected. On the contrary, breaks in the zones of the catalyst pattern instead result in connections in the silicon and contribute with mechanical stability to the zone plate mold. Connects between the metal catalyst zones are called "positive supports", whereas breaks in the metal catalyst zones are called "negative supports" (shown in Figure 5.2). Different investigated designs and their influence on the MACE outcome are discussed in Chapter 6. The zone plates were designed using the Raith_GDSII MATLAB toolbox that generates patterns compatible with Raith EBL systems [81].

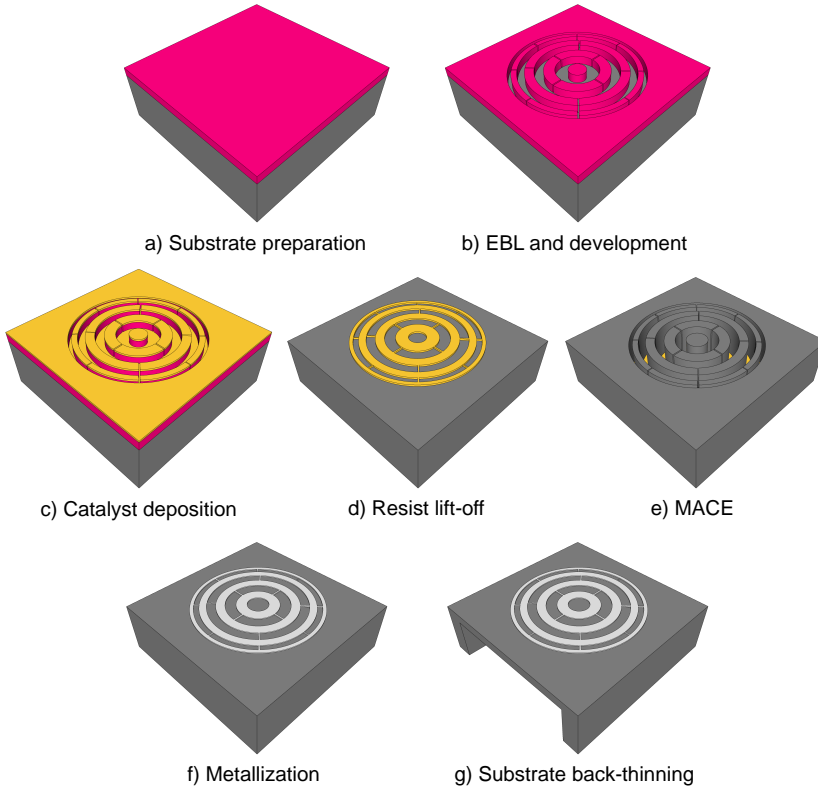


Figure 5.1. Overview of the zone plate nanofabrication process. a) Silicon substrate (dark grey) preparation by spin-coating 80 nm CSAR 62 e-beam resist (pink). b) Zone plate patterning by EBL and development for removal of resist residues. c) Deposition of 2 nm titanium and 10 nm gold (yellow) by evaporation. d) Lift-off of resist layer leaving the metal zone plate pattern only. e) Transferring the metal zone plate pattern into the substrate via MACE. f) Metallizing (light grey) the silicon mold via ELD or ED. g) Back-thinning the substrate via RIE. Figure adapted from Paper C.

The methacrylate-based e-beam resist CSAR 62 from Allresist GmbH was mainly used in this thesis. A thickness of 80 nm was typically spin coated on clean 1.5 cm x 1.5 cm silicon substrates. The size of the substrates were chosen to provide a large enough area with an even resist thickness for the zone plates to be exposed, as well as for easy handling throughout the fabrication process. The resist spin-coating was followed by 60 s baking on a 180°C hot plate. Thanks to the high sensitivity of CSAR 62 [82] and the

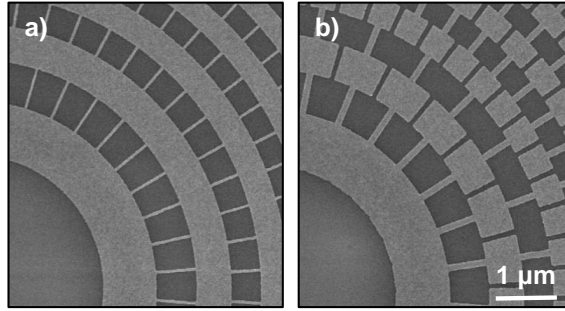


Figure 5.2. SEM micrographs of innermost parts of zone plates picturing a) positive and b) negative supports, respectively. Same scale bar applies to both micrographs.

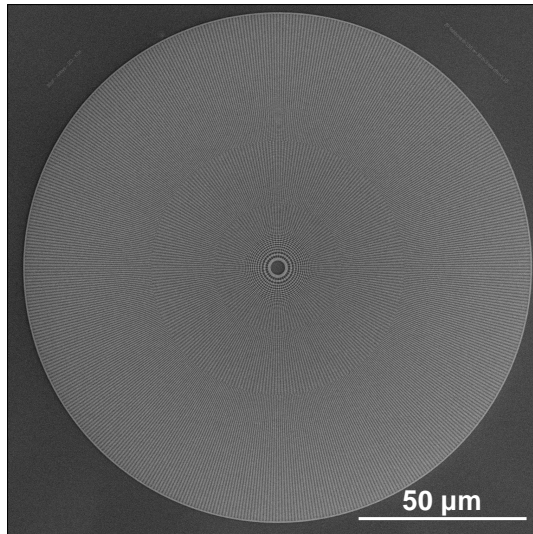


Figure 5.3. Zone plate design in gold on silicon. The gold acts as the catalyst in a later MACE step. The zone plate design diameter is 150 μm and outermost zone width is 30 nm.

high electron current of the used 50 kV Raith Voyager system, each zone plate with a 150 μm diameter, 1:1 line-to-space ratio and 30 nm outermost zone width took in average 3 min to expose. A zone plate pattern with such dimensions is pictured in Figure 5.3. An observation on the CSAR 62 resist is its tendency to leave residues in the pattern after development in amyl

acetate, even with a clearance dose. A short, 13 s oxygen plasma ashing step was therefore found necessary to remove all the remaining resist in the exposed areas for proper metal adhesion to the silicon substrate.

Gold was used as the MACE catalyst throughout this work. The metal deposition was performed using a custom in-house Eurovac/Thermionics electron-beam evaporator. Since gold does not adhere directly to the oxide layer present on the silicon substrate surface, an adhesive 2 nm titanium film was evaporated at 1 Å/s right before the gold deposition. It should be noted that the titanium layer immediately dissolves in HF when exposed to the etching solution and does not take part in the MACE process [83]. A gold thickness of 10 nm was chosen and evaporated at 2 Å/s. The choice on the gold thickness was based on a few considerations. Firstly, the thinner the resist layer the easier the resist lift-off, especially in the outermost parts of the zone plate pattern where the zones are as small as 30 nm. Secondly, a thicker gold film would require a thicker resist layer, too. If the gold film is too thick in relation to the resist thickness, the deposited gold will connect to gold on top of the resist forming bridges and the lift-off will fail. The resist thickness affects the stability of the pattern, especially in the outermost parts of the zone plate pattern. When the resist got thicker than 80 nm, the smallest exposed features tended to collapse after development, as is shown in Figure 5.4. Lastly, a gold thickness of 10 nm is within the range of previously reported catalyst thicknesses for optics fabrication [49, 51].

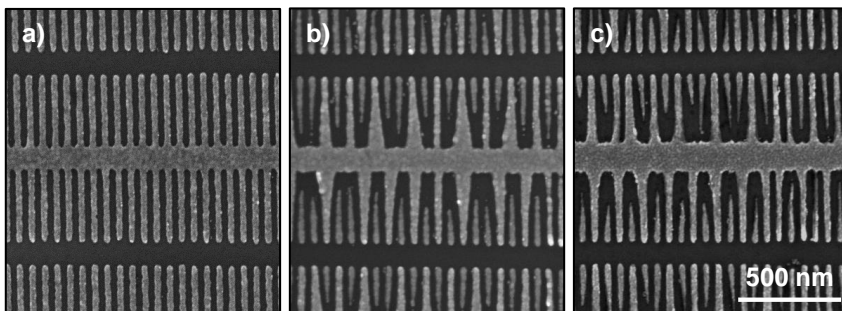


Figure 5.4. SEM micrographs gold zone plate patterns (outermost parts) after CSAR 62 lift-off with thicknesses a) 80 nm, b) 130 nm and c) 200 nm. The scale bar applies to all three micrographs.

The resist lift-off was performed in dimethyl succinate and included several sequences of high power ultrasonication. Before the actual lift-off, some preparatory steps were found to be especially important for a successful process. Directly after the metal deposition, the substrates were left to soak in dimethyl succinate for at least 12 hours. Right before the ultrasonica-

tion, the most part of the metal coated resist was stripped away in acetone and then put on a 80°C hot plate for 10 min. Both the long soaking time and pre-heating resulted in a highly effective process. The ultrasonication was performed for 10 min and the substrates were then put back on the hot plate for 10 more minutes. The heating/ultrasonication in dimethyl succinate was repeated in total three times. Finally, the substrates were transferred to isopropanol and thereafter to deionized water (DI H₂O) and ultrasonicated for an additional 10 min in each solvent. The total time required for the entire lift-off process was approximately one hour.

5.2 Pattern transfer with metal-assisted chemical etching

This section describes the practicalities of a typical MACE process used in this thesis (Figure 5.1 e)). The investigation of different experimental parameters and their effect on the etching outcome is presented in Chapter 6. Silicon wafers of p-type (100) with boron doping and resistivity of 1–5 $\Omega \cdot \text{cm}$ were used for the most part throughout this work. The thickness of the wafers was 250 μm . For the study of silicon doping effect on zone plate etching p-type (100), boron doped wafers with a resistivity of 0.001–0.005 $\Omega \cdot \text{cm}$ were additionally used. The latter silicon-type was further used for the proof of concept of ED metalization.

The MACE reaction is initiated on the surface of the gold catalyst (Chapter 4). Therefore, it is of high significance that the substrate surface, and especially the gold surface, is free from adsorbed organics and other impurities that might prevent the etching from starting. A 3 min oxygen plasma cleaning step was introduced right before the MACE to ensure a reproducible process.

A typical etching solution consisted of HF, H₂O₂ and DI H₂O and was freshly prepared before each experiment. The MACE was performed in a polytetrafluoroethylene container under light protection to exclude any influence from surrounding illumination [84]. All experiments were conducted using an etching solution volume of 15 ml to ensure the abundance of reactants. The clean substrates were mounted on the bottom of the container to prevent any movement that might disrupt the etching. When the influence of temperature on the etching was assessed, pre-temperature regulated chemicals were used to prepare the etching solution and the MACE was performed using a Lauda Eco RE620 Silver thermostat and bath for temperature control. The etching was initiated after temperature stabilization of both the substrate and the etching solution. Every investigated MACE condition was repeated at least three times.

After MACE, the substrates were rinsed in copious amounts of DI H₂O and transferred to ethanol. The samples were critical point dried over 20

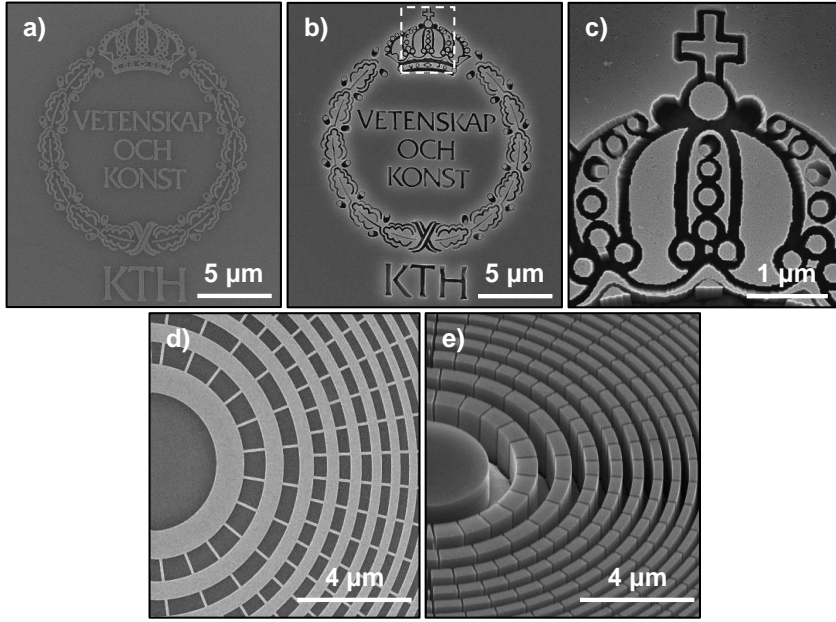


Figure 5.5. SEM micrographs of gold patterned silicon pre- and post-MACE. KTH logo a) pre-MACE and b) post-MACE. c) pictures the inset in b) where the difference in the MACE outcome of smaller and larger structures is clear. The smallest circular details in the KTH crown show a broader tendency to collapse compared to the larger circles. An interconnected zone plate pattern with positive supports is shown in d) pre-MACE and e) post-MACE. Adapted from Paper B.

cycles using a Leica EM CPD300. Figure 5.5 pictures examples of MACE processed patterns.

5.3 Metalization methods

Until now, the nanofabrication of silicon zone plate molds has been described. As explained in Chapter 3, the use of high-Z materials is advantageous from a fabrication point of view for the zone plates to function at hard X-ray wavelengths. In this section, two different plating methods to metallize silicon zone plate molds with palladium and gold are presented (Figure 5.1 f)).

5.3.1 Palladium electroless deposition

The palladium deposition was performed using ELD [85, 86]. Commonly, a metal complex, reducing agent and bath stabilizers are the main components in an ELD plating bath. In the autocatalytic process of ELD, the metal complex is selectively reduced on a conductive surface. The reduced and deposited metal now acts as a catalyst in the process and the metal buildup continues on the same site. For the metalization of silicon molds, a selective deposition on the gold at the bottom of the etched zone plate structures is desired. Therefore, as a preparatory step, a 3 min oxygen plasma treatment was performed to passivate the silicon surface by oxidation. This way, any palladium deposition on other sites than the catalytic gold layer was prevented (see Figure 5.6). The plasma treatment also added to the hydrophilic character and thus easier wetting of the gold surface. Contact angle measurements revealed a change from 89° to 29° due to adsorbed oxygen or presence of an oxide layer on the gold surface [87, 88].

The PD-Tech PC electroless Pd system from Atotech was used for the palladium deposition. A fresh 100 ml plating bath was prepared for each sample to ensure process reliability and the plating was performed under magnetic stirring at 120 rpm. Inductively coupled plasma optical emission spectrometry (ICP-OES) measurements revealed a palladium concentration of 5 mM per plating bath. The plating temperature was set to 40°C and the process was initiated when immersing the substrate into the plating bath. In early plating experiments, the substrates were sitting vertically in

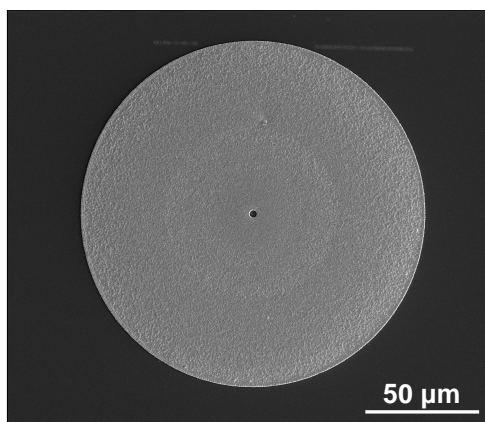


Figure 5.6. SEM micrograph of ELD metallized palladium/silicon zone plate. The palladium is selectively deposited in the zone plate area. Figure adapted from Paper C.

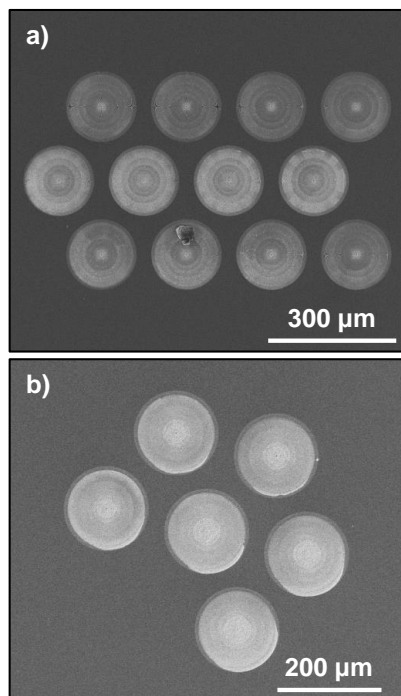


Figure 5.7. SEM micrographs of palladium plated zone plates using different setups. In a) the substrate was sitting in a holder at the bottom of the plating bath. The zone plates are not plated, completely plated and semi-plated in the top, middle and bottom row, respectively. In b) the substrate was immersed into the bath from the top which resulted in homogeneous plating of all zone plates.

a holder at the bottom of the plating bath. This experimental setup resulted in uneven plating over single zone plates and complete or no plating of zone plates on the same substrate. Instead, the setup was changed so that the substrates were immersed into the plating bath from the top which resulted in a more homogeneous plating, as pictured in Figure 5.7.

For a zone plate to reach its maximum theoretical efficiency, the density of the zone plate material should be close to the tabulated density of the material. The tabulated density value for palladium is 12 g/cm^3 . The density was assessed from plated films by gravimetric analysis and transmission measurements. Samples were prepared similarly to the zone plates, but instead a predefined area of $1.5 \text{ cm} \times 1.5 \text{ cm}$ plating base (2 nm titanium adhesion layer and 10 nm gold) on silicon substrates were plated. The gravimetric analysis was performed by measuring the weight of the plated

films and relating it to the volume of the films by measuring their thicknesses. For this an analytical scale and a surface profilometer were used. The average density of three plated films were $10.7 \pm 0.4 \text{ g/cm}^3$.

The transmission measurements were conducted at beamline 6-2c at the Stanford Synchrotron Radiation Lightsource. The transmission at 9 keV of three $30 \mu\text{m} \times 30 \mu\text{m}$ points per plated film was compared to three reference points on the same chip. Relating the thickness of the films to the transmitted photons, the density of the palladium films were calculated. The average density calculated from transmission data of three plated films were $10.9 \pm 0.2 \text{ g/cm}^3$. Both measurements show a lower palladium density than the theoretical value. The incorporation of relatively light-weight elements in the bath formulation, such as brighteners, and the presence of pores or voids in the plated metal would be reasons for this [89]. Figure 5.8 pictures a palladium metallized zone plate. The efficiency characterization of these palladium/silicon zone plates is presented in Chapter 7.

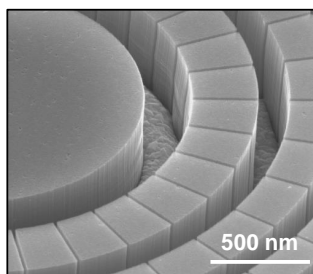


Figure 5.8. SEM micrograph showing the innermost part of a partly palladium plated silicon zone plate.

5.3.2 Gold electrodeposition

Another way to selectively metallize the zone plate mold is through ED [90]. The essential components in the ED process are a cathode, an anode or counter electrode and the plating solution that holds the metal complex to be plated in a stable and reducible form [91]. A current is applied to the cathode, in this case the substrate holding the zone plate molds, which attracts the surrounding metal complexes. Upon polarization of the metal complex in the electric field, the ligand gets stripped off and the metal gets deposited on the charged cathode surface [89]. The silicon surface was passivated through a 3 min oxygen plasma treatment to avoid any deposition off-site the zone plate structures. The ED was performed at 50°C in a 8 ml plating bath based on gold sulphite from Schütz Dental GmbH. From ICP-OES measurements the gold content in the bath was determined to be

70 mM. In Figure 5.9 we demonstrate the proof of concept of selective gold ED of a MACE processed zone plate.

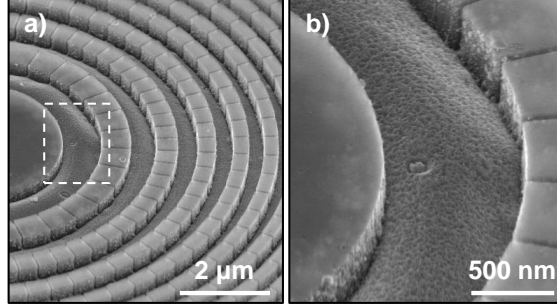


Figure 5.9. SEM micrographs of gold plated zone plate. The plating time was 1 min and the applied current 15 μA . b) shows a magnification of the inset area in a).

5.4 Substrate back-thinning

The zone plate substrate needs to be more or less transparent to the incoming X-rays. A 250 μm thick silicon substrate, as used in this work, only transmits 7.8 % of 9 keV light. While a thick substrate is robust and easy to handle, it requires thinning down to be used as a device. Furthermore, the thinned-down substrate needs to have a uniform thickness over the zone plate area to ensure the same phase-shift throughout the entire zone plate. The silicon substrate back-thinning makes the final part of the zone plate nanofabrication process (Figure 5.1 g)).

For this, a two-step deep reactive ion etching (DRIE) was used [92]. As a preparation, the positive photoresist Microposit S1813 was spin-coated on both the back of the silicon chip and the zone plate front for protection. Using the Smartprint optical maskless lithography system, circular sites at the back parts of the zone plates were defined and the photoresist was developed for 60 s in Microposit MF-319 developer. Chromium was deposited by thermal evaporation to act as an etch mask during the DRIE and the resist was removed in a lift-off process in acetone under sonication.

The first step was a cryogenic DRIE step at -50°C followed by a second short DRIE step at 30°C for polishing purposes. The etching was performed in a gas mixture of sulfur hexafluoride (SF_6), oxygen (O_2) and fluoroform (CHF_3) [93]. An etch rate of 9 $\mu\text{m}/\text{min}$ was obtained with this process. Figure 5.10 shows a cross-section of a thinned down and polished substrate.

The silicon substrates were thinned down to 25 μm which resulted in an improvement to 78 % transmission of 9 keV X-rays.

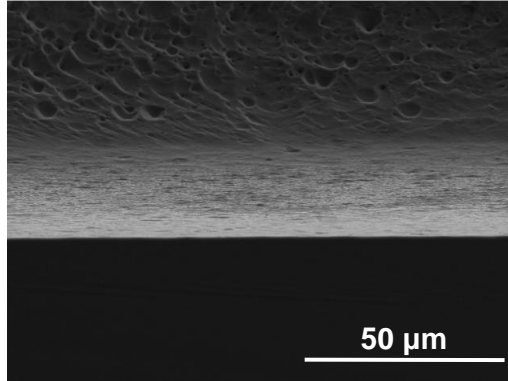


Figure 5.10. SEM micrograph of a thinned down silicon substrate cross-section prepared with the presented DRIE process. Figure adapted with permission from F. Lundberg [92].

Chapter 6

Optimization of metal-assisted chemical etching for zone plate nanostructures

With MACE as the pattern transfer method, hard X-ray zone plate optics fabrication has taken a new turn. Since the first study in 2014 [49], the number of publications has rapidly increased [9]. The reasons for the interest in MACE for hard X-ray optics fabrication is the capability of the method to fabricate ultra-high aspect ratio silicon nanostructures while being relatively simple and low-cost [15, 52].

High-aspect ratio silicon structures are desired for both resolution and focusing efficiency purposes. For fabrication of a good quality zone plate, there are important morphological characteristics that need to be maintained during MACE. In order to diffract the photons into the correct orders with high efficiency, the etched silicon zones must be vertical and mechanically stable. This is especially important for a successful metalization of the silicon mold in a later fabrication step. Another important morphological aspect is the surface of the zone sidewalls. The walls must be dense and smooth to avoid any focusing efficiency loss and to obtain the aimed resolution of the device [94].

Based on the morphological characteristics mentioned above, this chapter describes the experimental investigation about the influence of the MACE parameters presented in Chapter 4 on zone plate etching. The effect of etching solution and temperature on the reaction kinetics is discussed, different zone plate designs are studied in terms of etching verticality and mechanical stability of the silicon nanostructures and the effect of silicon resistivity on silicon wall roughness is shown. Papers A, B and D were mainly based on the work presented in this chapter.

6.1 Etching solution composition

At relatively high HF concentrations, the oxidant in the etching solution is the MACE rate determining reactant [60]. We investigated the kinetic and morphological effects of the oxidant H_2O_2 by systematically increasing its concentration while keeping the HF concentration constant. The experimental parameters for this study are listed in Table 6.1.

Table 6.1. Investigated MACE conditions for the study of etching solution composition influence on zone plate etching. The HF concentration ($[\text{HF}]$), temperature (T), etch time (t), outermost zone width (Δr) and silicon resistivity (ρ_{Si}) were kept constant. An etching time series was performed with the etching solution composition containing 0.68 M H_2O_2 .

$[\text{H}_2\text{O}_2] : [\text{HF}]$ (M)	T ($^{\circ}\text{C}$)	t (min)	Δr (nm)	ρ_{Si} ($\Omega \cdot \text{cm}$)
0.17 : 4.7	25	4	100	1-5
0.34 : 4.7	25	4	100	1-5
0.68 : 4.7	25	4, 8, 16, 32	100	1-5
1.4 : 4.7	25	4	100	1-5

As pictured in Figure 6.1 a)-c), dense and smooth silicon zones were obtained up to a H_2O_2 concentration of 0.68 M. The investigated H_2O_2 concentrations up to this point gave a linear etch trend where 0.17 M, 0.34 M, 0.68 M resulted in $\approx 0.70 \mu\text{m}$, $\approx 1.3 \mu\text{m}$ and $\approx 2.6 \mu\text{m}$ etch depths, respectively. This trend did not continue at the highest studied H_2O_2 concentration of 1.4 M. At this concentration, the zones appeared rough, indicating porosity, and the etch depth was only $\approx 0.87 \mu\text{m}$ (Figure 6.1 d)). A comparative atomic force microscopy (AFM) study using a Bruker FastScan system in tapping mode showed that the surface roughness of the third zone at 0.68 M H_2O_2 and 1.4 M H_2O_2 were 0.56 nm rms and 2.3 nm rms, respectively.

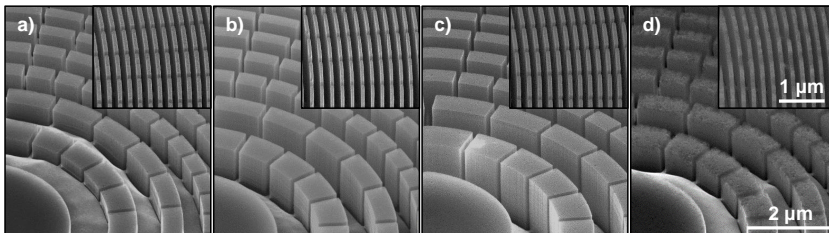


Figure 6.1. Effect of etching solution composition. Zone plates etched at H_2O_2 concentrations of a) 0.17 M, b) 0.34 M, c) 0.68 M and d) 1.4 M and a constant HF concentration of 4.7 M. Same scale bars apply to main SEM micrographs and the insets. The insets show the outermost zones. Figure adapted from Paper A.

Based on the suggested MACE theory in Chapter 4, this etching behaviour can be explained as the kinetics of hole injection and consumption reactions being in or out of balance. With increasing H_2O_2 concentration the formation of holes at the gold surface also increases which leads to a faster hole injection rate and thus a higher hole density at the gold/silicon interface. When the silicon dissolution reaction rate is in balance with the hole injection rate, all holes are consumed at the gold/silicon interface and the etching behaviour is linear. When, however, the hole injection rate is faster than the silicon dissolution a surplus of unconsumed holes can diffuse into the silicon zones and result in a randomized etching behaviour. This effect might be enhanced by our interconnected zone plate design with positive supports, where every silicon pillar is surrounded by the gold catalyst which to a larger extent might contribute to off-site etching. Since the etching solution with 0.68 M H_2O_2 gave the most profound etch depth with maintained dense and smooth zone walls, it was used for further investigations of achievable etch depths in a time study.

The optimized etching solution composition together with an interconnected zone plate catalyst design were seemingly not limiting in terms of achievable etch depths (see Figure 6.2). The etching trend was linear (≈ 0.7 $\mu\text{m}/\text{min}$) indicating an abundance of chemicals in the etching solution with an effective replenishment of reactants at the catalytic sites. The pH value

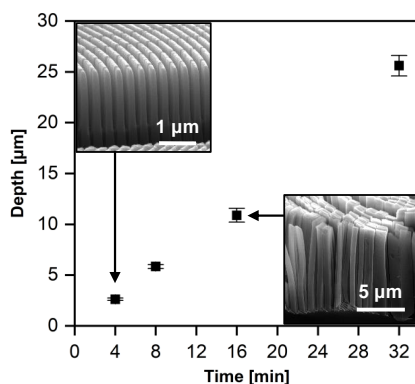


Figure 6.2. Zone plate etch depth as a function of etch time, based on cross-section SEM micrograph analysis. The error bars represent the standard deviation of etch depth measurements along the zone plate profile. The MACE processing was performed with an etching solution containing 0.68 M H_2O_2 . The top-left inset shows zone plate structures etched for 4 min. The cross-section was made by focused ion beam (FIB) milling. The bottom-right inset shows zone plate structures etched for 16 min. The cross-section was prepared by manual cleaving. Figure from Paper A.

was maintained throughout the whole time study showing that the consumption of HF in the MACE process was negligible with respect to the large etching solution volume (pH= 0–0.5). A vertical etching direction was maintained with the interconnected zone plate catalyst design, however as the bottom-right inset in Figure 6.2 depicts, collapse of zones became an issue at large etch depths due to free-standing silicon pillars. The silicon zone plate structures were stable up to 8 min etching at an etch depth of $\approx 6 \mu\text{m}$. The effect of different zone plate designs is further explored in 6.3.

6.2 Processing temperature

To understand how the MACE processing temperature affects the reaction kinetics and morphology of silicon structures, the influence of the etching solution temperature was investigated. For this, the etching solution with 0.68 M H_2O_2 was used. The experimental details for the temperature study are listed in Table 6.2.

Table 6.2. Investigated MACE conditions for the study of processing temperature influence on zone plate etching. The etching solution composition ($[\text{H}_2\text{O}_2] : [\text{HF}]$), etch time (t), outermost zone width (Δr) and silicon resistivity (ρ_{Si}) were kept constant.

T (°C)	$[\text{H}_2\text{O}_2] : [\text{HF}]$ (M)	t (min)	Δr (nm)	ρ_{Si} ($\Omega \cdot \text{cm}$)
10	0.68 : 4.7	4	100	1-5
25	0.68 : 4.7	4	100	1-5
40	0.68 : 4.7	4	100	1-5

Figure 6.3 a) shows that etching at 10 °C, which was the lowest investigated temperature, resulted in the smallest etch depth ($\approx 0.32 \mu\text{m}$). This can be attributed to slower hole injection and silicon dissolution rates at lower temperatures. As presented in the previous section, room temperature processing resulted in considerably deeper etching ($\approx 2.6 \mu\text{m}$, Figure 6.3 b)). Etching at 40 °C, the highest temperature studied, did not result in a larger etch depth than room temperature processing ($\approx 1.2 \mu\text{m}$, Figure 6.3 c)). In addition, the silicon structures had a rough appearance and AFM measurements revealed a surface roughness of 3.8 nm rms (0.56 nm rms at room temperature etching). This suggests that the hole injection and consumption reaction kinetics are out of balance and a diffusion of surplus holes to the surrounding silicon pillars.

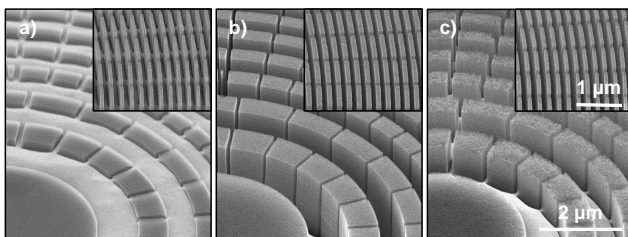


Figure 6.3. Influence of etching temperature. Zone plates etched at a) 10 °C, b) 25 °C and c) 40 °C. Same scale bars apply to main SEM micrographs and the insets. The insets show the outermost zones. Figure adapted from Paper A.

6.3 Zone plate catalyst design

While a grid-like, interconnected zone plate catalyst design contributes to a vertical etching direction, the resulting free-standing silicon structures limit the achievable zone heights due to collapse of the structures. This is especially noticeable at the outer parts of the zone plate where the zone widths are the smallest. One of the biggest challenges in MACE is to maintain a vertical etching profile of isolated catalysts [95, 96]. Therefore, though a zone plate catalyst with completely isolated zones (only gold rings) in theory will contribute to mechanical stability, the etching verticality will be an issue. A hybrid catalyst design with partly connected, partly interrupted zones could therefore be a good solution to obtain mechanically stable silicon structures while maintaining etching verticality. We designed three different zone plate catalysts with outermost zone widths of 30 nm, two interconnected and one hybrid (see Figure 6.4), and investigated their

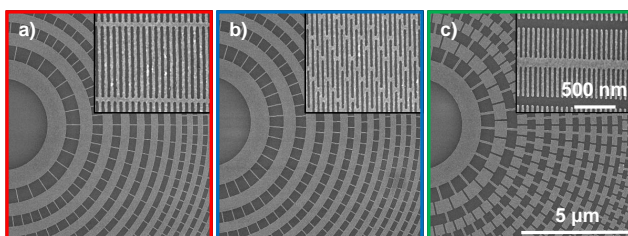


Figure 6.4. Zone plate gold catalyst designs. a) Net (red frame), b) brick wall (blue frame) and c) fishbone (green frame). In the net and brick wall designs the zones are interconnected, resulting in a grid-like pattern. In the fishbone design the zones are partly connected, partly isolated. Same scale bars apply to main SEM micrographs and the insets. The insets show the outermost zones. Figure adapted from Paper D.

respective etching behaviour at four different MACE conditions (C1-C4). The experimental MACE conditions are presented in Table 6.3.

Table 6.3. Investigated MACE conditions for the study of different zone plate designs. Four etch time (t) points per MACE condition was investigated. The outermost zone widths (Δr) and silicon resistivity (ρ_{Si}) were kept constant.

Condition	$[H_2O_2]:[HF]:[IPA]$ (M)	T (°C)	t (min)	ρ_{Si} ($\Omega \cdot cm$)
C1	0.68 : 4.7 : 0	25	3, 6, 9, 12	1-5
C2	0.068 : 4.7 : 0	25	3, 6, 9, 12	1-5
C3	0.68 : 4.7 : 0	8	3, 6, 9, 12	1-5
C4	0.68 : 4.7 : 0.91	25	3, 6, 9, 12	1-5

The net zone plate design (Figure 6.4 a)) has interconnects going transversely over all zones, while the interconnects in the brick wall design (Figure 6.4 b)) are shifted by half the line length. The shift of the interconnects was included to investigate any advantages from a stability aspect. In the fishbone hybrid design, the noble metal rings are interrupted forming sections with perpendicular lines crossing each section (Figure 6.4 c)).

The optimized etching solution composition presented in 6.1 (C1) was used as a starting point in the catalyst design study. Figure 6.5 a) shows a similar etching behaviour for all three designs with $\approx 2.5 \mu m$ etch depths. Both the net and brick wall designs had collapsed silicon structures in their outermost parts. While the fishbone catalyst design showed an overall even etching behaviour, the etching direction deviated from a vertical path due to the free gold ends. This was particularly visible in the outermost zones.

We investigated the relationship between MACE reaction kinetics and etching behaviour of our three catalyst designs. The H_2O_2 was lowered ten times (C2) to slow down the hole injection rate. As shown in Figure 6.5 b), a slower hole injection rate did not necessarily result in a homogeneous and controlled etching. Deformation of all catalysts was more apparent here than with any other investigated MACE condition. In fact, some parts within the same zone plate catalyst did not etch at all, while neighbouring zones did (see Figure 6.6 a)). The resulting etch depth was ≈ 500 nm and surprisingly, at this shallow etch depth collapse of the outermost zones was observed for both interconnected designs. The outermost zones of the fishbone design indicated a deviated etch direction with some of the zones straight and others not. This was also confirmed from the cross-section micrograph in Fig. 6.6 b). We attribute this etching behaviour to a limited access of H_2O_2 and an uneven distribution over the zone plate catalyst area. It should be noted that we did not mix our etching solution during MACE, which might explain the uneven etching behaviour at low H_2O_2 concentrations.

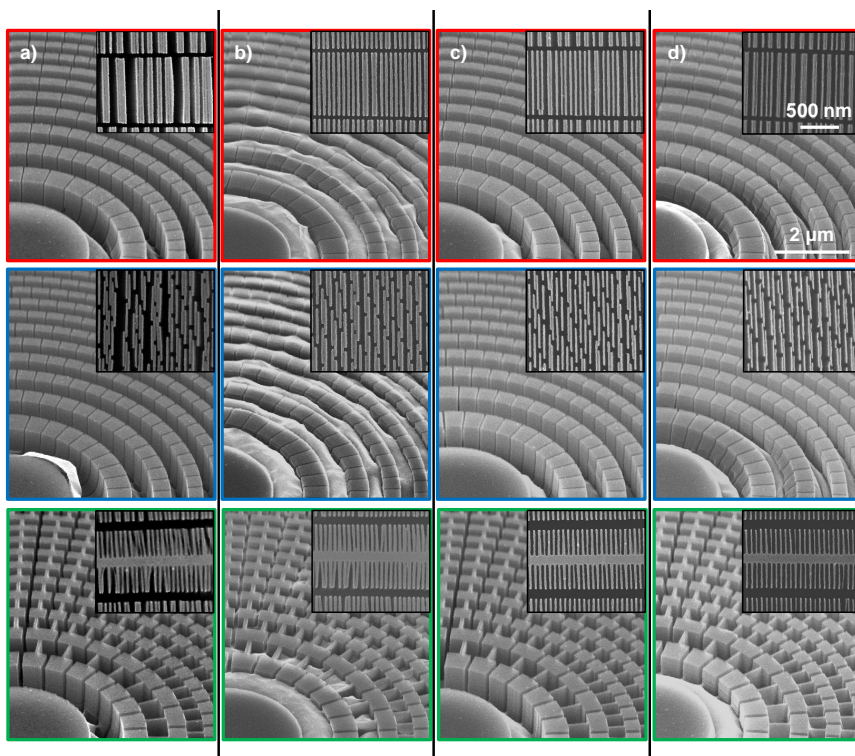


Figure 6.5. Net (red frame), brick wall (blue frame) and fishbone (green frame) zone plate designs etched for 6 min at MACE conditions a) C1, b) C2, c) C3 and d) C4. Same scale bars apply to main SEM micrographs and the insets. The insets show the outermost zones. Figure adapted from Paper D.

As an additional study on the MACE reaction kinetics influence on the etching behaviour, the temperature was lowered to 8°C (C3). An etch depth of $\approx 1.7 \mu\text{m}$ was observed at this lower processing temperature. Even though the difference in etch depth between the zone plates processed with conditions C2 and C3 is quite big, a lower processing temperature was more advantageous from a zone stability perspective. In Figure 6.5 c) the outermost zones in both the brick wall and fishbone designs were more stable while the collapse of zones was slightly more in the net design.

Alcohol addition to the etching solution has a reportedly positive effect on the etching uniformity and reduction of silicon wall roughness while slowing down the etch rate [71,97]. We investigated the effect of IPA addition to the etching solution (C4) and found a relatively smaller etch depth than without any solvent addition (cp. C1). The etch depth was $\approx 1.4 \mu\text{m}$.

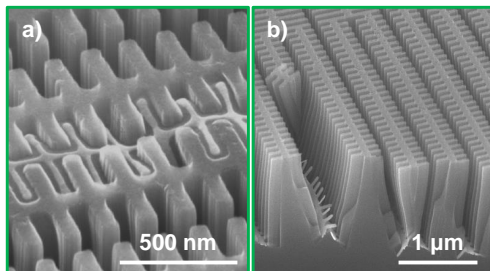


Figure 6.6. MACE inhomogeneity at too low H_2O_2 concentrations. Fishbone zone plate catalyst etched at MACE condition C2. SEM micrographs show a) local etching differences (6 min MACE) and b) non-vertical etching (12 min MACE). The cross-section in b) was prepared by manual cleaving. Figure adapted from Paper D.

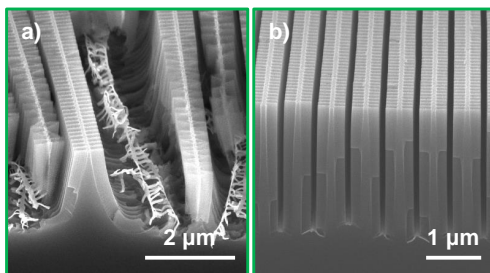


Figure 6.7. The effect of IPA on etching verticality. The fishbone zone plate design processed for 9 min with MACE conditions a) C1 and b) C4. The cross-sections were made by cleaving. Figure adapted from Paper D.

Slight broadening of the innermost zones was observed for both interconnected designs, see Figure 6.5 d). Nonetheless, the addition of IPA improved the etching uniformity of the fishbone design. Figure 6.7 illustrates cross-section micrographs of the fishbone catalyst design etched with conditions C1 and C4. The presence of IPA clearly prevented the non-vertical movement of the catalyst under the etching so that a more linear translation into the substrate was achieved.

6.4 Silicon type

On the contrary to ELD, metalization of silicon zone plate molds via ED depends on the conductivity of the silicon substrate. A more conductive substrate is a better suited cathode for ED than a substrate with higher re-

sistivity. Therefore, the influence of silicon resistivity on MACE was studied. The experimental parameters are listed in Table 6.4.

Table 6.4. Investigated MACE conditions for the study of silicon resistivity (ρ_{Si}) on zone plate etching. The etching solution composition ($[\text{H}_2\text{O}_2] : [\text{HF}]$), temperature (T), etch time (t) and outermost zone width (Δr) were kept constant.

ρ_{Si} ($\Omega \cdot \text{cm}$)	$[\text{H}_2\text{O}_2] : [\text{HF}]$ (M)	T ($^{\circ}\text{C}$)	t (min)	Δr (nm)
1-5	0.68 : 4.7	25	4	100
0.001-0.005	0.68 : 4.7	25	4	100

The higher the resistivity of a silicon substrate, the lower the conductivity and hence, the lower the dopant concentration. Two substrates with resistivities 1-5 $\Omega \cdot \text{cm}$ and 0.001-0.005 $\Omega \cdot \text{cm}$ were chosen for this study. Figure 6.8 shows the noteworthy difference between two zone plates etched into these substrates.

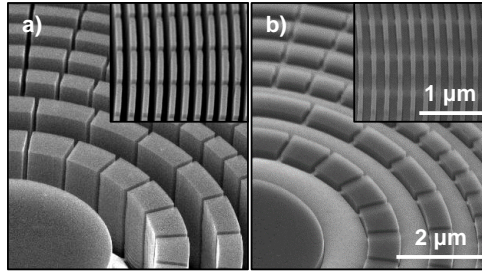


Figure 6.8. Influence of silicon doping concentration. Zone plates etched using p-type (100), boron doped silicon with resistivity a) 1-5 $\Omega \cdot \text{cm}$ and b) 0.001-0.005 $\Omega \cdot \text{cm}$. Same scale bars apply to the SEM micrographs in a) and b). The insets show the outermost zones.

The silicon substrate with resistivity 1-5 $\Omega \cdot \text{cm}$ had an etch depth of $\approx 2.6 \mu\text{m}$, while substrate with resistivity 0.001-0.005 $\Omega \cdot \text{cm}$ had an etch depth of only $\approx 0.32 \mu\text{m}$. Roughly, a factor of eight longer etching time would be needed with the 0.001-0.005 $\Omega \cdot \text{cm}$ resistivity silicon to reach the same etch depths as the 1-5 $\Omega \cdot \text{cm}$ resistivity silicon.

As briefly mentioned in Chapter 4, the silicon porosity was expected to increase with dopant concentration [76]. In Figure 6.9 high magnification micrographs depict isolated gold catalyst etched into a silicon substrate with 0.001-0.005 $\Omega \cdot \text{cm}$ resistivity. Pores in the silicon started to appear after 4 min etching. This etching behaviour suggests that hole injection is facilitated and the rate is increased with a higher dopant concentration. A competing etching mechanism to the catalyst etching might be a possible

explanation to the relatively shallow etch depth obtained for the zone plates resulting in a higher degree of porosity.

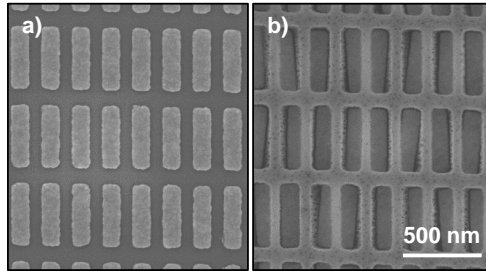


Figure 6.9. Isolated gold test structures etched using p-type (100), boron doped silicon with resistivity $0.001\text{-}0.005\ \Omega \cdot \text{cm}$, a) pre-MACE and b) after 4 min MACE. Same scale bars apply to both SEM micrographs.

Chapter 7

Zone plate efficiency characterization

In Chapter 5 the nanofabrication process of palladium/silicon zone plates using MACE as the pattern transfer method and ELD as the palladium metalization method were presented. The fabricated palladium/silicon zone plates were characterized at the NanoMAX beamline at MAX IV by quantifying their first order diffraction efficiency. This chapter covers a description of the experimental setup used for the characterization and discusses and compares the obtained results with the calculated theoretical data. The first order diffraction efficiency measurement was the main zone plate characterization method presented in Paper C.

7.1 Experimental setup

A coherent hard X-ray beam with 9 keV photon energy was used for the quantification of the zone plate first order diffraction efficiency. Several zone plates were analyzed and all had outermost zone widths of 30 nm and zone heights of 900 nm, i.e., aspect ratios of 30:1. Their diameters were 150 μm . Interconnected zone plate designs were chosen, both net and brick, for best zone verticality during MACE (for the designs, see Chapter 6). The general characterization setup is shown in Figure 7.1. The main components in the experimental arrangement included a 25 μm -wide and 25 μm -thick tungsten central stop (CS), a 10 μm order sorting aperture (OSA) and a Crycam X-ray camera from Crytur. The optical components in the setup were aligned with software-controlled three-axis piezoelectric nanopositioning stages. The OSA was placed slightly upstream the zone plate focal plane, which in turn was placed at an equal distance to the camera. For the first order diffraction efficiency quantification, images of

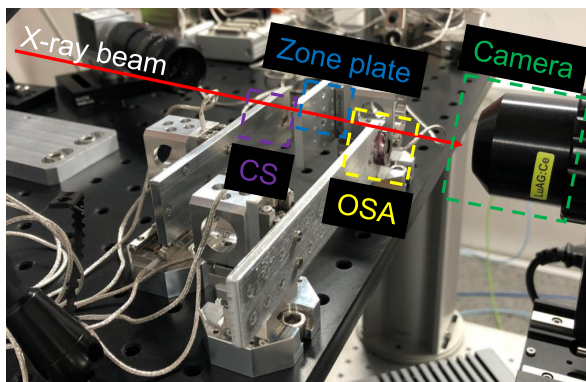


Figure 7.1. Photograph of the experimental setup that was used for zone plate first order diffraction efficiency measurements at NanoMAX. The main components are indicated.

the first order zone plate cone and the empty beam transmitted through the silicon substrate without the zone plate and OSA were recorded. The focusing efficiency was calculated by relating the photons in focus to the total number of photons transmitted through the silicon substrate.

7.2 First order diffraction efficiency quantification

For a combined palladium/silicon zone plate the maximum theoretical efficiency of 30% would be expected at $3\text{ }\mu\text{m}$ zone height (see Figure 7.2). This is given that the phase-shifting palladium is of 12 g/cm^3 bulk density. At 900 nm zone height our interconnected zone plate designs proved mechanical stability to the outermost 30 nm zones. Larger zone heights caused collapse of the free-standing silicon nanostructures. A palladium/silicon zone plate at 900 nm zone height has a theoretical first order diffraction efficiency of 6.4% . Both gravimetric and transmission analyses of the ELD plated palladium indicated a density within the range of $10\text{--}11\text{ g/cm}^3$, i.e., a lower palladium density than the tabulated bulk value (for details on the palladium density measurements, see Chapter 5). As Figure 7.2 depicts, with a decreasing palladium density, a decrease in zone plate efficiency was expected. The theoretical first order diffraction efficiency at 10 g/cm^3 and 11 g/cm^3 should be 4.0% and 5.1% , respectively.

The best total efficiency measured of our 900 nm thick zone plate devices at 9 keV was 1.9% . The difference from the theoretical efficiency is attributed to several factors. Primarily, the main decrease in efficiency can be explained by the tilting effect of the outermost parts of the zone plate.

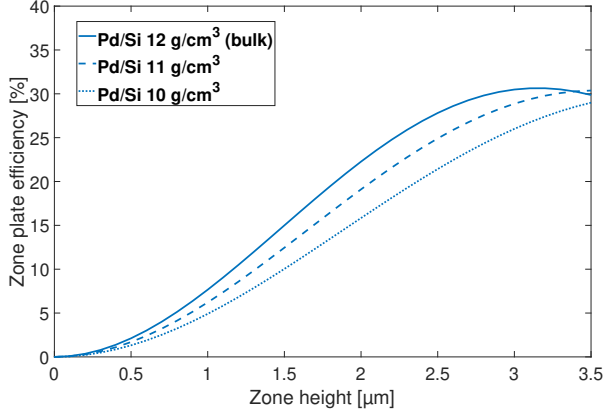


Figure 7.2. Palladium density impact on the zone plate efficiency. First order diffraction efficiency as function of zone height for palladium/silicon zone plates at 9 keV photon energy. A lower palladium density than bulk (12 g/cm^3) results in lower efficiency at a specific zone height. Bulk silicon density was chosen for the calculations. Calculations were done in MATLAB using GD-Calc [38].

Figure 7.3 shows an image of the first order zone plate cone, which is a map of the local diffraction efficiency. The intensity drop indicates that tilting of zones started at about $1/3$ of the radius, with decreasing intensity toward the edges. This is confirmed by Figure 7.4 that shows cross-section micrographs along the zone plate radius. The zones in the outer part are clearly more tilted than the inner and middle zones. Additionally, the interconnects in our zone plate design add to an efficiency drop. While the interconnects are advantageous concerning etching verticality in MACE, they reduce the effective zone plate area. The palladium over plating also has a minor effect on the deviating efficiency outcome due to some absorption of photons. The net and brick interconnected designs showed similar efficiencies of 1.9% and 1.8 %, respectively.

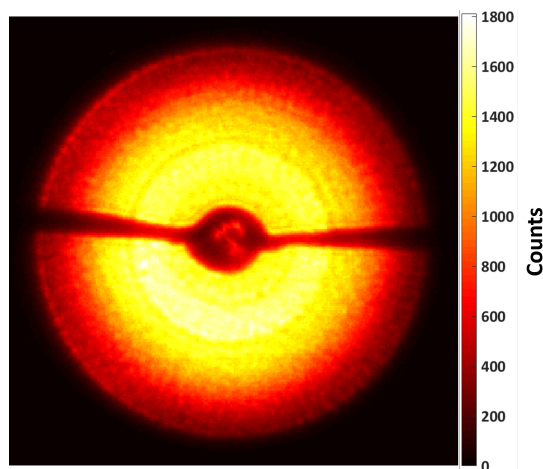


Figure 7.3. Image of the first order diffraction cone showing the local palladium/silicon zone plate efficiency. The measurement was performed at the NanoMAX beamline at MAX IV. Figure from Paper C.

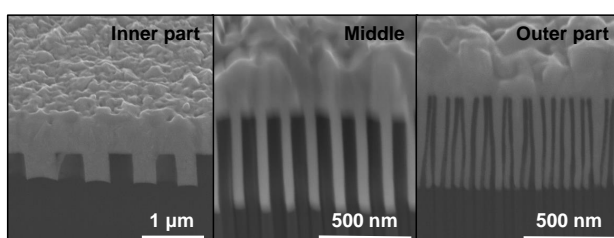


Figure 7.4. SEM micrographs of FIB milled cross-sections of inner, middle and outer parts of a palladium/silicon zone plate radius. The narrow zones in the outermost parts of the zone plate are slightly tilted. Figure adapted from Paper C.

Chapter 8

Conclusions and outlook

X-ray zone plates are today among the most challenging devices to fabricate due to the requirement of high-aspect ratio nanostructures. This thesis presents a detailed exploration of MACE for the nanofabrication of hard X-ray zone plates and includes both investigations on method optimization and development of a new nanofabrication process.

For the MACE optimization, the main conclusions were the following:

- Etching verticality could be maintained with an interconnected, grid-like catalyst design. No careful control of the MACE kinetics was needed for this. The achievable aspect ratios were however limited by the mechanical stability of the free-standing silicon nanostructures.
- Mechanical stability of the silicon nanostructures were achieved with a partly interconnected, partly isolated hybrid catalyst design. The vertical etching of the isolated parts of this design required carefully controlled MACE conditions. Both a low processing temperature and alcohol addition to the etching solution were beneficial for a maintained pattern integrity during MACE.
- The silicon wall roughness could be controlled by the MACE reaction kinetics. Preferable etching solution composition and processing temperature were identified to obtain dense and smooth silicon structures. In addition, a high silicon substrate resistivity was shown to benefit the silicon morphology. The higher the silicon resistivity, the deeper the catalytic etching and the smoother the silicon walls.

In the developed zone plate nanofabrication process the following were achieved:

- A silicon zone plate mold with aspect ratio 30:1, 30 nm smallest zone width and 150 μm diameter was fabricated using the optimized MACE

process. Today, 30 nm zone widths are among the smallest zone plate nanostructures reported with MACE as a nanofabrication process.

- An autocatalytic process, ELD, was used to selectively metallize the silicon zone plate molds with palladium. The gold catalyst used in MACE was in ELD used as a plating base for the palladium to deposit and grow on. Both MACE and ELD are conceptually simple, relatively low-cost and accessible processes that facilitate the zone plate device nanofabrication.
- At 9 keV, the fabricated zone plates had a first order diffraction efficiency of 1.9%.

In summary, this thesis work has shown the possibilities and pointed out some limitations of using MACE in the nanofabrication of hard X-ray zone plates. For future work, we hope to see that MACE has taken its place as a standardized method for the fabrication of high-quality nanofocusing optics. Apart from improvements on the smallest achievable zone width, a diffraction efficiency as close as possible to the theory is desirable. In this work, vertical etching was achieved with supports (positive and negative) in the catalyst design, which unfortunately reduced the effective zone plate area. Vertical, collective etching of isolated zones would overcome this efficiency loss and could be accomplished with external guidance of the catalyst during the MACE process. Magnetic-field [98,99] or electric-field [100,101] guided MACE could be introduced for zone plate nanofabrication.

Moving towards all-wet processing for the nanofabrication of zone plates is another potential progress in the field that does not seem too far away. Imagine dipping your metal patterned silicon substrate in a series of baths and in the end collect an etched and metallized zone plate device ready to be installed in a hard X-ray nanoprobe. This would save the X-ray scientist working with nanofabrication a lot of time. We have introduced palladium metalization with ELD and demonstrated gold metalization with ED, but additional metals using these methods should be explored to make this process available for a wider X-ray energy range.

In the end, it will be exciting to follow the development of X-ray microscopy. A dream scenario for many researchers would be to gather information about their samples with atomic resolution, both on the sample exterior and interior. For this to come true, further research on process development for nanofabrication of high quality optics is a must.

Summary of papers

This thesis is based on the five papers listed below, all relating to zone plate nanofabrication using MACE. The author was the main responsible for Papers A, B, C and D, including planning of the work, performing experiments, characterization, analysis of results and writing of the manuscripts. In Paper E, the author was involved in the planning and execution of MACE experiments. The zone plate gold patterning and SEM analysis in Papers A and B were performed by others.

Paper A: Reaction control of metal-assisted chemical etching for silicon-based zone plate nanostructures

This paper optimizes the reaction conditions for MACE of zone plate nanostructures. The effect of etching solution composition, temperature and etching time were investigated using interconnected zone plate patterns with 100 nm smallest zone widths. Parameter influence on etching directionality, silicon wall roughness, etching rate and zone height were explored.

Paper B: Investigation of metal-assisted chemical etching for fabrication of silicon-based X-ray zone plates

In this paper, early results from the optimization of zone plate processing with MACE are presented. The impact of etching solution composition, temperature and reaction time were studied here.

Paper C: Metal-assisted chemical etching and electroless deposition for fabrication of hard X-ray Pd/Si zone plates

The optimized MACE conditions in Paper A were used for the nanofabrication of palladium/silicon zone plate devices. For the first time, ELD was used for the metalization of the silicon zone plate molds. The fabricated zone plates had aspect ratios of 30:1 and outermost zone widths of 30 nm.

Paper D: Optimization of metal-assisted chemical etching for deep silicon nanostructures

As a continuation of the study in Paper A, this paper systematically studies the impact of zone plate designs in MACE. Here, interconnected and partly connected, partly isolated hybrid zone plate patterns were processed and the effect of etching solution composition, temperature and alcohol addition were investigated. Using this parameter space, the etching directionality and mechanical stability of the silicon zones were optimized. The zone plate patterns had outermost zone widths of 30 nm.

Paper E: High-aspect ratio zone plate fabrication for hard X-ray nanoimaging

This paper provides an overview of MACE for zone plate nanofabrication. Critical points of MACE for pattern transfer were identified and the potential and limitations of the process were discussed.

Acknowledgements

With my sincere gratitude, I would like to acknowledge a number of people without whom this work would not have been possible.

First and foremost, my supervisor Ulrich Vogt. You have always encouraged me to explore my ideas and supported me in every possible way. Coming from a different background to work on an interdisciplinary project was challenging at first, but standing at the end of the road I know I would not have it any other way. This is thanks to the friendly and inspiring atmosphere you created that made every day of this five-year journey a fun learning experience.

I would also like to extend my deepest gratitude to Muhammet Toprak. Muhammet hocam, your door was always open and your support endless. I loved our daily coffee and Turkish delight breaks combined with interesting discussions about research and life in general. You are a true friend and role model.

All members of the X-ray Optics and Nano Imaging group that I have gotten the chance to work with. Thomas Frisk, Stylianos Giakoumidis, Victoria Kim, Fabian Lundberg, Hanna Ohlin, Karolis Parfeniukas, Jussi Rahomäki and Mattias Åstrand – you all contributed to a great work environment and I have learned from each and every one of you.

Furthermore, I wish to thank every single colleague at BioX for making it such a warm and friendly workplace. Especially Hans Hertz, for his great leadership and for bringing together all sharp “tutti frutti” competences under the same roof. I’ve enjoyed every fika pause at BioX and the fun discussions that came with them. This is the best work place any PhD student could ask for.

A special thanks to Anne Sakdinawat for welcoming me in her group. I feel honored to have been a part of such an exciting project and to have met so many brilliant minds during my stay at SLAC. Kenan Li, thank you for your guidance in the laboratory, it was a pleasure working with you. Also, I would like to thank David Attwood for our nice and friendly discussions.

All staff members of the Albanova Nanolab, KTH Nanochemistry Lab and Stanford Nano Shared Facilities that made my work much easier.

Many thanks to Kian Shaker and Muhammet Toprak for proofreading this thesis.

Thanks to Ulf Johansson, Alexander Björling, Sebastian Kalbfleisch and everyone else at NanoMAX for all their support during the characterization experiment of my zone plates.

A big thanks to Adem Ergül for his guidance and kind help over the years.

Last but not least, thanks to all my family and friends who have been here for me with love and support along this journey. Especially to my parents, Gülcan and Kamil, and my brothers, Ahmet and Mahmut, for always encouraging and believing in me.

Bibliography

- [1] D. Fine, A. Grattoni, R. Goodall, S. S. Bansal, C. Chiappini, S. Hosali, A. L. van de Ven, S. Srinivasan, X. Liu, B. Godin, L. Brousseau, I. K. Yazdi, J. Fernandez-Moure, E. Tasciotti, H. J. Wu, Y. Hu, S. Klemm, and M. Ferrari, *Silicon micro- and nanofabrication for medicine*, Advanced Healthcare Materials **2**, 632–666 (2013).
- [2] K. Yamada, *Silicon Photonic Wire Waveguides: Fundamentals and Applications BT - Silicon Photonics II: Components and Integration*, pages 1–29, Springer Berlin Heidelberg, Berlin, Heidelberg (2011).
- [3] K. Balasundaram, P. K. Mohseni, Y.-C. Shuai, D. Zhao, W. Zhou, and X. Li, *Photonic crystal membrane reflectors by magnetic field-guided metal-assisted chemical etching*, Applied Physics Letters **103**, 214103 (2013).
- [4] G. Schierning, *Silicon nanostructures for thermoelectric devices: A review of the current state of the art*, Physica Status Solidi (a) **211**, 1235–1249 (2014).
- [5] F. Priolo, T. Gregorkiewicz, M. Galli, and T. F. Krauss, *Silicon nanostructures for photonics and photovoltaics*, Nature Nanotechnology **9**, 19–32 (2014).
- [6] E. Garnett and P. Yang, *Light trapping in silicon nanowire solar cells*, Nano Letters **10**, 1082–1087 (2010).
- [7] M. R. Zamfir, H. T. Nguyen, E. Moyen, Y. H. Lee, and D. Pribat, *Silicon nanowires for Li-based battery anodes: A review*, Journal of Materials Chemistry A **1**, 9566–9586 (2013).
- [8] Y. Yang, W. Yuan, W. Kang, Y. Ye, Q. Pan, X. Zhang, Y. Ke, C. Wang, Z. Qiu, and Y. Tang, *A review on silicon nanowire-based anodes for next-generation high-performance lithium-ion batteries from a material-based perspective*, Sustainable Energy Fuels **4**, 1577–1594 (2020).

- [9] L. Romano and M. Stampanoni, *Microfabrication of X-ray optics by metal assisted chemical etching: A review*, *Micromachines* **11**, 589 (2020).
- [10] L. Boarino and G. Amato, *Nanostructures Based on Porous Silicon BT - Encyclopedia of Nanotechnology*, pages 1–13, Springer Netherlands, Dordrecht (2014).
- [11] L. T. Canham, *Silicon quantum wire array fabrication by electrochemical and chemical dissolution of wafers*, *Applied Physics Letters* **57**, 1046–1048 (1990).
- [12] D. Dimova-Malinovska, M. Sendova-Vassileva, N. Tzenov, and M. Kamenova, *Preparation of thin porous silicon layers by stain etching*, *Thin Solid Films* **297**, 9–12 (1997).
- [13] X. Li and P. W. Bohn, *Metal-assisted chemical etching in HF/H_2O_2 produces porous silicon*, *Applied Physics Letters* **77**, 2572–2574 (2000).
- [14] M. Li, Y. Li, W. Liu, L. Yue, R. Li, Y. Luo, M. Trevor, B. Jiang, F. Bai, P. Fu, Y. Zhao, C. Shen, and J. M. Mbengue, *Metal-assisted chemical etching for designable monocrystalline silicon nanostructure*, *Materials Research Bulletin* **76**, 436–449 (2016).
- [15] H. Han, Z. Huang, and W. Lee, *Metal-assisted chemical etching of silicon and nanotechnology applications*, *Nano Today* **9**, 271–304 (2014).
- [16] Z. Huang, N. Geyer, P. Werner, J. De Boor, and U. Gösele, *Metal-assisted chemical etching of silicon: A review*, *Advanced Materials* **23**, 285–308 (2011).
- [17] J. L. Soret, *Ueber die durch Kreisgitter erzeugten Diffraction-sphänomene*, *Annalen der Physik* **232**, 99–113 (1875).
- [18] D. Attwood and A. Sakdinawat, *X-Rays and Extreme Ultraviolet Radiation*, Cambridge University Press, Cambridge (2016).
- [19] A. Sakdinawat and D. Attwood, *Nanoscale X-ray imaging*, *Nature Photonics* **4**, 840–848 (2010).
- [20] P. Kirkpatrick and A. V. Baez, *Formation of optical images by X-rays*, *Journal of the Optical Society of America* **38**, 766–774 (1948).
- [21] H. Mimura, H. Yumoto, S. Matsuyama, Y. Sano, K. Yamamura, Y. Mori, M. Yabashi, Y. Nishino, K. Tamasaku, T. Ishikawa, and K. Yamauchi, *Efficient focusing of hard X rays to 25nm by a total reflection mirror*, *Applied Physics Letters* **90**, 51903 (2007).

- [22] A. Björling, S. Kalbfleisch, M. Kahnt, S. Sala, K. Parfeniukas, U. Vogt, D. Carbone, and U. Johansson, *Ptychographic characterization of a coherent nanofocused X-ray beam*, Optics Express **28**, 5069–5076 (2020).
- [23] S. Suehiro, H. Miyaji, and H. Hayashi, *Refractive lens for X-ray focus*, Nature **352**, 385–386 (1991).
- [24] A. G. Michette, *No X-ray lens*, Nature **353**, 510 (1991).
- [25] A. Snigirev, V. Kohn, I. Snigireva, and B. Lengeler, *A compound refractive lens for focusing high-energy X-rays*, Nature **384**, 49–51 (1996).
- [26] C. G. Schroer, M. Kuhlmann, U. T. Hunger, T. F. Günzler, O. Kurapova, S. Feste, F. Frehse, B. Lengeler, M. Drakopoulos, A. Somogyi, A. S. Simionovici, A. Snigirev, I. Snigireva, C. Schug, and W. H. Schröder, *Nanofocusing parabolic refractive X-ray lenses*, Applied Physics Letters **82**, 1485–1487 (2003).
- [27] K. Saitoh, K. Inagawa, K. Kohra, C. Hayashi, A. Iida, and N. Kato, *Fabrication and characterization of multilayer zone plate for hard X-rays*, Japanese Journal of Applied Physics **27**, L2131–L2133 (1988).
- [28] A. V. Baez, *Fresnel zone plate for optical image formation using extreme ultraviolet and soft X radiation*, Journal of the Optical Society of America **51**, 405–412 (1961).
- [29] J. Kirz, *Phase zone plates for X rays and the extreme UV*, Journal of the Optical Society of America **64**, 301–309 (1974).
- [30] H. Yan, H. C. Kang, R. Conley, C. Liu, A. T. Macrander, G. B. Stephenson, and J. Maser, *Multilayer Laue lens: A path toward one nanometer X-ray focusing*, X-Ray Optics and Instrumentation **2010**, 401854 (2010).
- [31] M. Holt, R. Harder, R. Winarski, and V. Rose, *Nanoscale hard X-ray microscopy methods for materials studies*, Annual Review of Materials Research **43**, 183–211 (2013).
- [32] B. Kaulich, P. Thibault, A. Gianoncelli, and M. Kiskinova, *Transmission and emission X-ray microscopy: Operation modes, contrast mechanisms and applications*, Journal of Physics: Condensed Matter **23**, 83002 (2011).

- [33] Y. Hwu, W. L. Tsai, B. Lai, J. H. Je, G. H. Fecher, M. Bertolo, and G. Margaritondo, *Using photoelectron emission microscopy with hard-X-rays*, Surface Science **480**, 188–195 (2001).
- [34] U. Johansson, U. Vogt, and A. Mikkelsen, *NanoMAX: A hard X-ray nanoprobe beamline at MAX IV*, X-Ray Nanoimaging: Instruments and Methods **8851**, 88510L (2013).
- [35] N. Martensson and M. Eriksson, *The saga of MAX IV, the first multi-bend achromat synchrotron light source*, Nuclear Instruments and Methods in Physics Research Section A: Accelerators, Spectrometers, Detectors and Associated Equipment **907**, 97–104 (2018).
- [36] A. Holmberg, *Nanofabrication of zone plate optics for compact soft X-ray microscopy*, Ph.D thesis, KTH Royal Institute of Technology (2006).
- [37] K. Parfeniukas, *High-aspect ratio nanofabrication for hard X-ray zone plates*, Ph.D thesis, KTH Royal Institute of Technology (2018).
- [38] K. C. Johnson, *Grating Diffraction Calculator (GD-Calc®)*, (2019).
- [39] S. Gorelick, J. Vila-Comamala, V. Guzenko, R. Mokso, M. Stambanoni, and C. David, *Direct e-beam writing of high aspect ratio nanostructures in PMMA: A tool for diffractive X-ray optics fabrication*, Microelectronic Engineering **87**, 1052–1056 (2010).
- [40] J. Zhu, Y. Chen, S. Xie, L. Zhang, C. Wang, and R. Tai, *Nanofabrication of 30 nm Au zone plates by e-beam lithography and pulse voltage electroplating for soft X-ray imaging*, Microelectronic Engineering **225**, 111254 (2020).
- [41] K. Jefimovs, J. Vila-Comamala, T. Pilvi, J. Raabe, M. Ritala, and C. David, *Zone-doubling technique to produce ultrahigh-resolution X-ray optics*, Physical Review Letters **99**, 264801 (2007).
- [42] I. Mohacsi, I. Vartiainen, B. Rösner, M. Guizar-Sicairos, V. A. Guzenko, I. McNulty, R. Winarski, M. V. Holt, and C. David, *Interlaced zone plate optics for hard X-ray imaging in the 10 nm range*, Scientific Reports **7**, 43624 (2017).
- [43] Y. Feng, M. Feser, A. Lyon, S. Rishton, X. Zeng, S. Chen, S. Sassolini, and W. Yun, *Nanofabrication of high aspect ratio 24nm X-ray zone plates for X-ray imaging applications*, Journal of Vacuum Science Technology B: Microelectronics and Nanometer Structures Processing, Measurement, and Phenomena **25**, 2004–2007 (2007).

- [44] S.-C. Gleber, M. Wojcik, J. Liu, C. Roehrig, M. Cummings, J. Vila-Comamala, K. Li, B. Lai, D. Shu, and S. Vogt, *Fresnel zone plate stacking in the intermediate field for high efficiency focusing in the hard X-ray regime*, Optics Express **22**, 28142 (2014).
- [45] S. Ali and C. Jacobsen, *Effect of tilt on circular zone plate performance*, Journal of the Optical Society of America. A, Optics, image science, and vision **37**, 374–383 (2020).
- [46] J. Reinspach, M. Lindblom, O. von Hofsten, M. Bertilson, H. M. Hertz, and A. Holmberg, *Cold-developed electron-beam-patterned ZEP 7000 for fabrication of 13 nm nickel zone plates*, Journal of Vacuum Science Technology B: Microelectronics and Nanometer Structures Processing, Measurement, and Phenomena **27**, 2593–2596 (2009).
- [47] K. Parfeniukas, J. Rahomäki, S. Giakoumidis, F. Seiboth, F. Wittwer, C. G. Schroer, and U. Vogt, *Improved tungsten nanofabrication for hard X-ray zone plates*, Microelectronic Engineering **152**, 6–9 (2016).
- [48] M. Lindblom, J. Reinspach, O. von Hofsten, M. Bertilson, H. M. Hertz, and A. Holmberg, *High-aspect-ratio germanium zone plates fabricated by reactive ion etching in chlorine*, Journal of Vacuum Science Technology B: Microelectronics and Nanometer Structures Processing, Measurement, and Phenomena **27**, L1–L3 (2009).
- [49] C. Chang and A. Sakdinawat, *Ultra-high aspect ratio high-resolution nanofabrication for hard X-ray diffractive optics*, Nature Communications **5**, 1–7 (2014).
- [50] R. Akan, T. Frisk, F. Lundberg, H. Ohlin, U. Johansson, K. Li, A. Sakdinawat, and U. Vogt, *Metal-assisted chemical etching and electroless deposition for fabrication of hard X-ray Pd/Si zone plates*, (2020).
- [51] K. Li, M. J. Wojcik, R. Divan, L. E. Ocola, B. Shi, D. Rosenmann, and C. Jacobsen, *Fabrication of hard X-ray zone plates with high aspect ratio using metal-assisted chemical etching*, Journal of Vacuum Science Technology B, Nanotechnology and Microelectronics: Materials, Processing, Measurement, and Phenomena **35**, 06G901 (2017).
- [52] X. Li, *Metal assisted chemical etching for high aspect ratio nanostructures: A review of characteristics and applications in photovoltaics*, Current Opinion in Solid State and Materials Science **16**, 71–81 (2012).

- [53] R. C. Tiberio, M. J. Rooks, C. Chang, C. F. Knollenberg, E. A. Dobisz, and A. Sakdinawat, *Vertical directionality-controlled metal-assisted chemical etching for ultrahigh aspect ratio nanoscale structures*, Journal of Vacuum Science Technology B, Nanotechnology and Microelectronics: Materials, Processing, Measurement, and Phenomena **32**, 06F101 (2014).
- [54] R. Akan, K. Parfeniukas, C. Vogt, M. Toprak, and U. Vogt, *Reaction control of metal-assisted chemical etching for silicon-based zone plate nanostructures*, RSC Advances **8** (2018).
- [55] R. Akan, K. Parfeniukas, C. Vogt, M. S. Toprak, and U. Vogt, *Investigation of metal-assisted chemical etching for fabrication of silicon-based X-ray zone plates*, Microscopy and Microanalysis **24**, 286–287 (2018).
- [56] K. Li, S. Ali, M. Wojcik, V. De Andrade, X. Huang, H. Yan, Y. Chu, E. Nazaretski, A. Pattammattel, and C. Jacobsen, *Tunable hard X-ray nanofocusing with Fresnel zone plates fabricated using deep etching*, Optica **7** (2020).
- [57] L. Romano, M. Kagias, J. Vila-Comamala, K. Jefimovs, L.-T. Tseng, V. A. Guzenko, and M. Stampanoni, *Metal assisted chemical etching of silicon in the gas phase: A nanofabrication platform for X-ray optics*, Nanoscale Horizons (2020).
- [58] M. Lebugle, F. Dworkowski, A. Pauluhn, V. A. Guzenko, L. Romano, N. Meier, F. Marschall, D. F. Sanchez, D. Grolimund, M. Wang, and C. David, *High-intensity X-ray microbeam for macromolecular crystallography using silicon kinoform diffractive lenses*, Applied Optics **57**, 9032–9039 (2018).
- [59] L. Romano, J. Vila-Comamala, K. Jefimovs, and M. Stampanoni, *High-aspect-ratio grating microfabrication by platinum-assisted chemical etching and gold electroplating*, Advanced Engineering Materials **22**, 2000258 (2020).
- [60] C. Chartier, S. Bastide, and C. Lévy-Clément, *Metal-assisted chemical etching of silicon in $\text{HF-H}_2\text{O}_2$* , Electrochimica Acta **53**, 5509–5516 (2008).
- [61] N. Geyer, B. Fuhrmann, Z. Huang, J. de Boor, H. S. Leipner, and P. Werner, *Model for the mass transport during metal-assisted chemical etching with contiguous metal films as catalysts*, The Journal of Physical Chemistry C **116**, 13446–13451 (2012).

- [62] X. H. Xia, C. M. A. Ashruf, P. J. French, and J. J. Kelly, *Galvanic cell formation in silicon/metal contacts: The effect on silicon surface morphology*, Chemistry of Materials **12**, 1671–1678 (2000).
- [63] K. Peng, A. Lu, R. Zhang, and S.-T. Lee, *Motility of metal nanoparticles in silicon and induced anisotropic silicon etching*, Advanced Functional Materials **18**, 3026–3035 (2008).
- [64] S. Chattopadhyay, X. Li, and P. W. Bohn, *In-plane control of morphology and tunable photoluminescence in porous silicon produced by metal-assisted electroless chemical etching*, Journal of Applied Physics **91**, 6134–6140 (2002).
- [65] L. Li, Y. Liu, X. Zhao, Z. Lin, and C.-P. Wong, *Uniform vertical trench etching on silicon with high aspect ratio by metal-assisted chemical etching using nanoporous catalysts*, ACS Applied Materials Interfaces **6**, 575–584 (2014).
- [66] A. Hiraki, *Low temperature reactions at Si/metal interfaces; What is going on at the interfaces?*, Surface Science Reports **3**, 357–412 (1983).
- [67] A. Cros, J. Derrien, and F. Salvan, *Catalytic action of gold atoms on the oxidation of Si(111) surfaces*, Surface Science **110**, 471–490 (1981).
- [68] L. Kong, B. Dasgupta, Y. Ren, P. K. Mohseni, M. Hong, X. Li, W. K. Chim, and S. Y. Chiam, *Evidences for redox reaction driven charge transfer and mass transport in metal-assisted chemical etching of silicon*, Scientific Reports **6**, 36582 (2016).
- [69] L. Romano, M. Kagias, K. Jefimovs, and M. Stampanoni, *Self-assembly nanostructured gold for high aspect ratio silicon microstructures by metal assisted chemical etching*, RSC Advances **6**, 16025–16029 (2016).
- [70] C. Chiappini, *MACE Silicon Nanostructures BT - Handbook of Porous Silicon*, pages 247–267, Springer International Publishing, Cham (2018).
- [71] L. Romano, J. Vila-Comamala, K. Jefimovs, and M. Stampanoni, *Effect of isopropanol on gold assisted chemical etching of silicon microstructures*, Microelectronic Engineering **177**, 59–65 (2017).
- [72] Y. Kim, A. Tsao, D. H. Lee, and R. Maboudian, *Solvent-induced formation of unidirectionally curved and tilted Si nanowires during*

- metal-assisted chemical etching*, Journal of Materials Chemistry C **1**, 220–224 (2013).
- [73] G. Sandu, J. Avila Osses, M. Luciano, D. Caina, A. Stopin, D. Bonifazi, J.-F. Gohy, A. Silhanek, I. Florea, M. Bahri, O. Ersen, P. Leclère, S. Gabriele, A. Vlad, and S. Melinte, *Kinked silicon nanowires: Superstructures by metal-assisted chemical etching*, Nano Letters **19**, 7681–7690 (2019).
 - [74] S. L. Cheng, C. H. Chung, and H. C. Lee, *A study of the synthesis, characterization, and kinetics of vertical silicon nanowire arrays on (001)Si substrates*, Journal of The Electrochemical Society **155**, D711 (2008).
 - [75] A. Backes, M. Leitgeb, A. Bittner, and U. Schmid, *Temperature dependent pore formation in metal assisted chemical etching of silicon*, ECS Journal of Solid State Science and Technology **5**, P653–P656 (2016).
 - [76] N. Geyer, N. Wollschläger, B. Fuhrmann, A. Tonkikh, A. Berger, P. Werner, M. Jungmann, R. Krause-Rehberg, and H. S. Leipner, *Influence of the doping level on the porosity of silicon nanowires prepared by metal-assisted chemical etching*, Nanotechnology **26** (2015).
 - [77] A. Backes and U. Schmid, *Impact of doping level on the metal assisted chemical etching of p-type silicon*, Sensors and Actuators, B: Chemical **193**, 883–887 (2014).
 - [78] A. Backes, A. Bittner, M. Leitgeb, and U. Schmid, *Influence of metallic catalyst and doping level on the metal assisted chemical etching of silicon*, Scripta Materialia **114**, 27–30 (2016).
 - [79] K. Balasundaram, J. S. Sadhu, J. C. Shin, B. Azeredo, D. Chanda, M. Malik, K. Hsu, J. A. Rogers, P. Ferreira, S. Sinha, and X. Li, *Porosity control in metal-assisted chemical etching of degenerately doped silicon nanowires*, Nanotechnology **23** (2012).
 - [80] J. Kim, H. Han, Y. H. Kim, S.-H. Choi, J.-C. Kim, and W. Lee, *Au/Ag bilayered metal mesh as a Si etching catalyst for controlled fabrication of Si nanowires*, ACS Nano **5**, 3222–3229 (2011).
 - [81] University of Alberta nanoFAB Centre, *Raith_GDSII MATLAB toolbox*, (2020).
 - [82] A. S. Gangnaik, Y. M. Georgiev, and J. D. Holmes, *New generation electron beam resists: A review*, Chemistry of Materials **29**, 1898–1917 (2017).

- [83] E. M. M. Sutter and G. J. Goetz-Grandmont, *The behaviour of titanium in nitric-hydrofluoric acid solutions*, Corrosion Science **30**, 461–476 (1990).
- [84] O. Volovlikova, S. Gavrilov, and P. Lazarenko, *Influence of illumination on porous silicon formed by photo-assisted etching of p-type Si with a different doping level*, (2020).
- [85] S. S. Djokić and P. L. Cavallotti, *Electroless Deposition: Theory and Applications BT - Electrodeposition: Theory and Practice*, pages 251–289, Springer New York, New York, NY (2010).
- [86] M. J. den Exter, *The use of electroless plating as a deposition technology in the fabrication of palladium-based membranes*, Woodhead Publishing Limited (2014).
- [87] D. Berman and J. Krim, *Impact of oxygen and argon plasma exposure on the roughness of gold film surfaces*, Thin Solid Films **520**, 6201–6206 (2012).
- [88] K. Sun, M. Kohyama, S. Tanaka, and S. Takeda, *Structures and stabilities of gold oxide films on gold surfaces in O₂ atmosphere*, Surface Science **628**, 41–49 (2014).
- [89] P. Wilkinson, *Understanding gold plating*, Gold Bulletin **19**, 75–81 (1986).
- [90] L. P. Bicelli, B. Bozzini, C. Mele, and L. D’Urzo, *A review of nanostructural aspects of metal electrodeposition*, International Journal of Electrochemical Science **3**, 356–408 (2008).
- [91] M. W. Losey, J. J. Kelly, N. D. Badgayan, S. K. Sahu, and P. S. Rama Sreekanth, *Electrodeposition BT - Reference Module in Materials Science and Materials Engineering*, Elsevier (2017).
- [92] F. Lundberg, *Membrane fabrication by dry silicon etching for X-ray optics*, M.Sc. thesis, KTH Royal Institute of Technology (2020).
- [93] R. Legtenberg, H. Jansen, M. de Boer, and M. Elwenspoek, *Anisotropic reactive ion etching of silicon using SF₆/O₂/CHF₃ gas mixtures*, Journal of The Electrochemical Society **142**, 2020–2028 (1995).
- [94] G. Schneider, *Influence of roughness and interdiffusion in zone plate structures on the diffraction efficiency described by coupled wave theory*, Applied Physics Letters **73**, 599–601 (1998).

- [95] L. Kong, Y. Zhao, B. Dasgupta, Y. Ren, K. Hippalgaonkar, X. Li, W. K. Chim, and S. Y. Chiam, *Minimizing isolate catalyst motion in metal-assisted chemical etching for deep trenching of silicon nanohole array*, ACS Applied Materials and Interfaces **9**, 20981–20990 (2017).
- [96] P. Lianto, S. Yu, J. Wu, C. V. Thompson, and W. K. Choi, *Vertical etching with isolated catalysts in metal-assisted chemical etching of silicon*, Nanoscale **4**, 7532–7539 (2012).
- [97] R. W. Wu, G. D. Yuan, K. C. Wang, T. B. Wei, Z. Q. Liu, G. H. Wang, J. X. Wang, and J. M. Li, *Bilayer-metal assisted chemical etching of silicon microwire arrays for photovoltaic applications*, AIP Advances **6**, 25324 (2016).
- [98] T. K. Kim, J.-H. Bae, J. Kim, Y.-C. Kim, S. Jin, and D. W. Chun, *Bulk micromachining of Si by annealing-driven magnetically guided metal-assisted chemical etching*, ACS Applied Electronic Materials **2**, 260–267 (2020).
- [99] Y. Oh, C. Choi, D. Hong, S. D. Kong, and S. Jin, *Magnetically guided nano-micro shaping and slicing of silicon*, Nano Letters **12**, 2045–2050 (2012).
- [100] X. Jiao, Y. Chao, L. Wu, and A. Yao, *Metal-assisted chemical etching of silicon 3D nanostructure using direct-alternating electric field*, Journal of Materials Science: Materials in Electronics **27**, 1881–1887 (2016).
- [101] P.-J. Chien, T.-C. Wei, and C.-Y. Chen, *High-speed and direction-controlled formation of silicon nanowire arrays assisted by electric field*, Nanoscale Research Letters **15**, 25 (2020).